TAMPEREEN TEKNILLINEN YLIOPISTO
TAMPERE UNIVERSITY OF TECHNOLOGY

KIM SANDVIK

SEARCHING FOR A CONDENSED RESONATING VALENCE BOND STATE IN CLUSTER MAGNETS

Master's thesis

Examiner: Prof. Esa Räsänen
Examiner and topic approved by the Faculty Council of the Faculty of Natural Sciences on 3rd February 2016

ABSTRACT

Kim Sandvik: Searching for a condensed resonating valence bond state in cluster magnets
Tampere University of Technology
Master of Science Thesis, 49 pages, 2 Appendix pages
August 2016
Master's Degree Programme in Science and Engineering
Major: Advanced Engineering Physics
Examiner: Professor Esa Räsänen

Keywords: frustration, antiferromagnet, resonating valence-bond state, $LiZn_2Mo_3O_8$, cluster magnet, neutron scattering

Frustrated quantum spin systems have been studied for quite some while. In frustrated systems such as in a triangular lattice all the spins cannot be simultaneously determined by antiferromagnetic interaction. In theory this will cause quantum fluctuations to switch the spin orientations, which leads to a quantum spin liquid (QSL) state. Various materials, for example edge-sharing tetrahedral or Kagome lattices have been proposed to be QSL candidates. Nonetheless, solid evidence has not been found for the QSL state in frustrated magnets.

A promising method to confirm the existence of a QSL state is inelastic neutron scattering. As a fermion the neutron has a spin magnetic moment of 1/2 and it will interact with unpaired spin magnetic moments. When this occurs, the neutron will lose some of its kinetic energy, which can be observed and interpreted as an excited quasi-particle, spinon.

This study focuses on an insulating cluster magnet $LiZn_2Mo_3O_8$, which has attracted a lot of attention recently. It contains Mo_3O_{13} clusters which are connected to each other by shared oxygen atoms. This leads to a Mo_3O_8 two-dimensional cluster plane of a hexagonal pattern. Each cluster has one unpaired electron contributing to a spin 1/2 magnetic moment. The electrons can interact antiferromagnetically with each other between the clusters. This is expected to be observed as a resonating valence bond (RVB) state – a type of a QSL state. The cluster planes are separated by layers of Li and Zn ions which provide the unpaired electron for each cluster. We believe that the full and evenly distributed occupation of Li and Zn sites tends to be imperfect in powder samples which could prevent the forming of the RVB state.

This thesis focuses on finding a solid state reaction recipe to synthesize a stoichiometric compound of $LiZn_2Mo_3O_8$. Also zinc hole doping dependence on lattice constants and magnetic susceptibility is studied. The analysis based on lithium is not in the scope of the thesis work as neutron powder diffraction (NPD) is required to obtain lithium lattice occupations. The magnetic susceptibility of some of the powder samples shows novel behavior for the $LiZn_2Mo_3O_8$ compound.

In this thesis $LiZn_2Mo_3O_8$ single-crystal growth is also done and specimens in the range of 100–900 microns were found. Further experiments are still needed to fully confirm that single-crystals of the correct compound were grown.

TIIVISTELMÄ

Kim Sandvik: Kondensoituneen resonoivan valenssisidostilan etsintä klusterimagneeteissa
Tampereen teknillinen yliopisto
Diplomityö, 49 sivua, 2 liitesivua
Elokuu 2016
Teknis-luonnontieteellinen koulutusohjelma
Pääaine: Teknillinen fysiikka
Tarkastaja: professori Esa Räsänen

Avainsanat: frustraatio, antiferromagneetti, resonoiva valenssisidostila, $LiZn_2Mo_3O_8$, klusterimagneetti, neutronisironta

Kvanttimekaanista frustraatiota on tutkittu jo jonkin aikaa. Frustroituneissa järjestelmissä kuten kolmiohiloissa kaikki spinin magneettiset momentit eivät voi yhtäaikaisesti olla määriteltyinä antiferromagneettisilla kahdenkeskisillä vuorovaikutuksilla. Teoriassa tämä aiheuttaa kvanttimekaanisten spinien jatkuvan suunnan vaihtumisen eli niin sanotun nesteenkaltaisen kvantti-spintilan (spin-nesteen) muodostumisen. Useita eri materiaaleja kuten tetraedrisiä tai Kagome-hiloja on ehdotettu spin-nestekandidaateiksi. Frustroituneille magneeteille tästä erityisestä kvanttitilasta ei ole vielä saatu riittävän vahvaa kokeellista näyttöä.

Epäelastinen neutronisironta on lupaava menetelmä, jolla spin-neste voidaan todentaa. Fermionina neutronilla on spin-1/2 magneettinen momentti, jolloin se voi vuorovaikuttaa vapaiden spinien kanssa. Näin tapahtuessa neutroni menettää osan kineettisestä energiastaan, mikä voidaan havaita ja tulkita virittyneenä kvasihiukkasena, spinonina.

Tämä työ keskittyy yhdisteeseen $LiZn_2Mo_3O_8$, joka on eriste sekä magneettinen atomirypäs, ns. magneettinen klusteri. Yhdiste on viime aikoina herättänyt paljon huomiota kiinteän olomuodon fysiikassa. Se sisältää Mo_3O_{13}-klustereita, jotka ovat sidoksissa toisiinsa jaettujen happiatomien kautta. Tämä saa aikaan kuusikulmaisia ja kaksiulotteisia Mo_3O_8-tasoja. Jokaisella klusterilla on yksi pariton elektroni, jolla on spin-1/2 magneettinen momentti. Nämä elektronit voivat vuorovaikuttaa antiferromagneettisesti keskenään klusterien välillä. Oletettavasti tämä on nähtävissä resonoivana valenssisidostilana, joka on eräs malli spin-nestetilalle. Klusteritasot ovat erotettuina toisistaan kerroksella Li- ja Zn-ioneja, jotka ovat vastuussa parittomien elektronien luovuttamisesta jokaiselle klusterille. Tutkimusryhmämme uskoo, että Li- ja Zn-miehityksellä on taipumus olla epätäydellisesti jakautunut sekä vajaa. Tämä voisi estää resonoivan valenssisidostilan muodostumisen.

Tässä työssä kehitettiin reseptiä ja menetelmää, joilla syntetisoidaan stoikiometrinen $LiZn_2Mo_3O_8$-näyte sekä tutkitaan sinkin vajauksen vaikutusta hilavakioihin ja magneettiseen suskeptibiliteettiin. Litiumin vajauksen vaikutusta ei voitu tutkia, koska litiumin miehitysten mittaaminen hilasta vaatii neutronidiffraktiokokeet, joihin ei tämän työn yhteydessä vielä ollut mahdollisuuksia. Joidenkin jauhenäytteiden magneettisessa suskeptibiliteetissa mitattiin ennennäkemätöntä käyttäytymistä $LiZn_2Mo_3O_8$-yhdisteelle. Tässä työssä kasvatettiin myös $LiZn_2Mo_3O_8$-yksittäiskiteitä suuruusluokaltaan 100–900 mikronia. Lisätutkimuksia tarvitaan vielä vahvistamaan tyhjentävästi, että löydetyt yksittäiskiteet todella ovat oikeaa yhdistettä.

PREFACE

This thesis work was carried out during my student exchange (2014–2015) in Japan at Tohoku University in the Quantum Spin Physics Laboratory, which belongs to the Division of Inorganic Material Research of the Institute of Multidisciplinary Research for Advanced Materials (IMRAM).

I feel indebted to all the laboratory members for accepting me as part of their research group. They patiently guided me in all the experimental work, of which I had non-existent previous experience. Especially I want to express my gratitude to my advisor Professor Taku J. Sato. He introduced me to the interesting research field of geometrically frustrated magnets and made his laboratory resources available to me.

I want to thank Doctor Maxim Avdeev of Australian Nuclear Science and Technology Organisation (ANSTO), who performed the neutron diffraction experiments in this work. I also want to thank Professor Esa Räsänen, who without previous knowledge of precisely this research topic, took up the role as the examiner of this thesis and helped me through the tedious writing task.

23 August 2016

Kim Sandvik

CONTENTS

LIST OF FIGURES

LIST OF SYMBOLS AND ABBREVIATIONS

ANSTO	Australian Nuclear Science and Technology Organisation
a	Lattice constant a-axis
b	Lattice constant b-axis
c	Lattice constant c-axis
C	Curie constant
Cj	Collimator
°C	Celsius degree
CGS	Centimeter-gram-second system
COLABS	Cooperative Laboratory Study Program
emu	Magnetic unit in the CGS system
ESR	Electron spin resonance
H	Magnetic field
H	Hamiltonian
HCl	Hydrochloride acid
ICP	Inductively coupled plasma
IMRAM	Institute of Multidisciplinary Research for Advanced Materials
In	Indium
INS	Inelastic neutron scattering
J	Exchange constant
K	Kelvin
Li	Lithium
M	Magnetization
Mo	Molybdenum
MPMS	Magnetic property measurement system
NMR	Neutron magnetic resonance
NPD	Neutron powder diffraction
O	Oxygen
Oe	Oersted
PPMS	Physical property measurement system
QSL	Quantum spin liquid
RVB	Resonating valence bond
S	Spin quantum number
S	Spin operator
Sc	Scandium
SEM	Scanning electron microscope
SQUID	Superconducting quantum interference device
T	Tesla
T_C	Curie temperature
VBS	Valence bond solid
XRD	X-ray powder diffraction
Z	Lattice multiplicity
Zn	Zinc
Å	Ångström
2θ	2Theta angle
λ	Wavelength
μSR	Muon spin rotation
φ	Phi angle

χ	Chi angle
χ	Magnetic susceptibility
χ_0	Diamagnetic contributions
χ^2	Chi-squared distribution
ψ	Wave function
ω	Omega angle

1. INTRODUCTION

Many interesting phenomena in solid state physics can be explained by quantum mechanics. Such examples are superconductivity and quantum tunneling to name a few. Also magnetism in materials can originate from electron spin magnetic moments which is a quantum mechanical property. These spin magnetic moments can be considered to be located in a specific pattern within a lattice of a crystalline material. Depending on how these spins align according to each other we can find different types of magnetism such as ferromagnetism, paramagnetism, or antiferromagnetism. The last one is of particular interest in this thesis: a phenomenon called geometrical frustration can be typically found in antiferromagnetic materials. In some special cases of these frustrated spin systems, exotic states such as spin ice, spin glass, or spin liquid [1] are expected to emerge.

Geometrically frustrated antiferromagnetic systems have been studied in condensed matter physics for quite some while [2, 3]. Magnetic disordering is expected even down to zero Kelvin in some systems like in the resonating valence bond (RVB) state. In the past decades there has been an increasing amount of experimental and theoretical activity in the study of frustrated magnetism for example in two-dimensional triangular [4], Kagome [5, 6], and tetrahedral [7] lattice systems.

This thesis is an experimental study on a frustrated antiferromagnet $LiZn_2Mo_3O_8$, which is a candidate for a condensed valence bond state. It has spin magnetic moments located in Mo_3O_8 clusters arranged in planes of the two-dimensional triangular pattern which forms a basis for geometrical frustration. This compound has recently attracted a lot of interest [8–14]. Our study as well as supplementary information of previous reports [8], [12] suggest that $LiZn_2Mo_3O_8$ tends not to be stoichiometric as shared Li/Zn cites are imperfectly occupied. As a result, Mo_3O_{13} clusters would be only partly magnetic, thus breaking the symmetry required for a geometrically frustrated system. Therefore, a major goal in this thesis is to find a way to create $LiZn_2Mo_3O_8$ with stoichiometric Li and Zn occupation, as well as to study the Li and Zn hole doping dependence, the effect of imperfect Li and Zn occupation, on physical properties like lattice constants and magnetic behavior.

Unlike in astrophysics for example, in condensed matter and solid state physics the samples for experimental studies have to be fabricated in a laboratory if good specimens cannot easily be found in nature. In this thesis, solid-state reaction methods were used to synthesize powder crystal samples and to grow single-crystals. Several more or less altered recipes of $LiZn_2Mo_3O_8$ were tried out to find the best recipe for a stoichiometric

powder sample and to carry out a study on the Li and Zn hole doping dependence. Also there were a few trials and errors until a success with a $LiZn_2Mo_3O_8$ single-crystal growth was achieved.

In this thesis powder X-ray diffraction (XRD) and the Rietveld analysis were crucial for quickly obtaining crystal data of newly produced powder samples and to verify that they are of the right compound. For single-crystal samples, 4-axis X-ray diffraction was used instead. A magnetic property measurement system (MPMS) magnetometer was used to obtain data of the magnetic behavior of the samples. Neutron powder diffraction (NPD) was done to several $LiZn_2Mo_3O_8$ samples in order to measure lithium occupancy, which could not be done reliably with XRD only. However, these results are not in the scope of this thesis work and will be published later [15] with the exception of preliminarily NPD results for one sample which were measured outside the actual beam time. The primary aim in studying $LiZn_2Mo_3O_8$ is to obtain conclusive experimental evidence of the existence a spin liquid state or resonating valence bond condensation. Inelastic neutron scattering (INS) seems to be a prominent method for achieving this. In the near future using the results of this work, INS will likely be performed on a $LiZn_2Mo_3O_8$ powder sample which is as stoichiometric as possible.

2. THEORY

In this chapter some basic and more advanced theoretical concepts in the scope of this thesis are explained. This work relies largely on concepts of solid-state physics and quantum mechanics. First, the valence bond and the corresponding theories are briefly explained since they relate with further topics. Then, antiferromagnetism and a phenomenon called geometrical frustration are reviewed. This phenomenon tends to emerge in materials showing antiferromagnetic behavior. The resonating valence bond (RVB) theory as a mechanism for a spin liquid is then explained. Finally, spinon quasiparticle excitations are discussed as they are expected to emerge in spin liquids.

2.1 Valence bond

In chemistry the definition for valence is the capacity of number of atoms and groups a single atom can unite chemically with. Usually this means that there are partially vacant electron orbitals with so called valence electrons. By overlapping these vacant orbitals of neighboring atoms the valence electrons can form a valence bond. In 1916 Lewis [16] proposed a bond that has two interacting electrons involved, known as the Lewis dot structure. In 1927 the Heitler–London [17] valence bond theory, which took quantum mechanics into account, was presented. A simple description of the valence bond wave function ψ is given by

$$\psi = \frac{1}{\sqrt{2}}(|\uparrow\downarrow\rangle + |\downarrow\uparrow\rangle), \tag{2.1}$$

where $|\uparrow\downarrow\rangle$ and $|\downarrow\uparrow\rangle$ are states of the electron pair spins. The arrows indicate that the spins in the states are opposite to each other. The two states are in a superposition with each other corresponding to a so-called zero spin singlet.

2.2 Antiferromagnetism

Magnetism in materials arises from magnetic moments which usually can be considered to be contributed by electron spins in vacant orbitals. Fully occupied orbitals have a net magnetic moment of zero due to the Pauli exclusion principle that allows only two spins of opposite spin to occupy the same state. There are a few ways how magnetic moments in the material may be aligned in relation to each other. A simple illustration of some of some of these are illustrated in Figure 1.

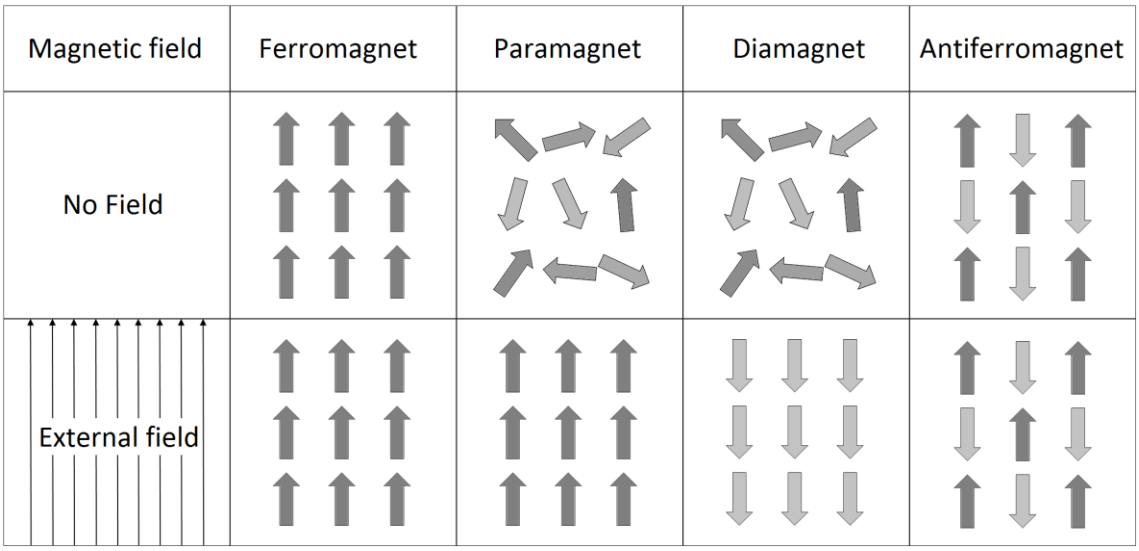

Figure 1. *Alignment of magnetic moments in different types of magnets with and without the influence of an external magnetic field.*

Ferromagnetism is the best known effect due to its everyday applications such as fridge magnets. Here the magnetic moments order spontaneously in the same direction without an external magnetic field. The magnetic field produced by the ferromagnet will strengthen (weaken) a parallel (antiparallel) magnet field. Paramagnets on the other hand have their magnetic moments randomly disordered in all directions but align according to an external magnetic field. Diamagnetism is similar to paramagnetism but the moments oppose the external field by aligning in the opposite direction. All materials are considered to have a varying amount of diamagnetic contribution.

In antiferromagnetic ordering the magnetic moments try to align in opposite directions to each other. This should not be confused with paramagnetism although both have zero magnetization in the absence of an external field. Antiferromagnets have a transition temperature called the Néel temperature where they usually turn into paramagnets when the thermal energy gets high enough to break the magnetic ordering into disorder.

Solid state physics has a great deal of interest in antiferromagnetism as it relates to topics that are yet to be conclusively explored and understood. For example, some high temperature superconductors are doped antiferromagnets and a phenomenon called geometrical frustration occurs especially in antiferromagnets. This is discussed in detail below.

2.3 Geometrical frustration

In physics the meaning of frustration is a state where competing forces cannot be simultaneously satisfied. Geometrical frustration emerges from symmetry. For example, in a symmetrical lattice spin magnetic dipole moments have many neighbors with whom to form valence bonds in an antiferromagnetic fashion. These possible bonds have the

same probability to form, and because of the wave nature of matter in quantum mechanics, they will be fluctuating in a superposition with each other. If the symmetry is broken for some reason in the lattice, the geometrical frustration might be lost as well. Geometrically frustrated lattices include triangular [4], Kagome [5, 6] and corner-sharing tetrahedral [7] lattices. Ramirez [18] presented the so called frustration parameter, a tool for evaluating the degree of frustration.

A simple example of geometrical frustration is a Ising spin antiferromagetic triangular lattice visualized in Figure 2.

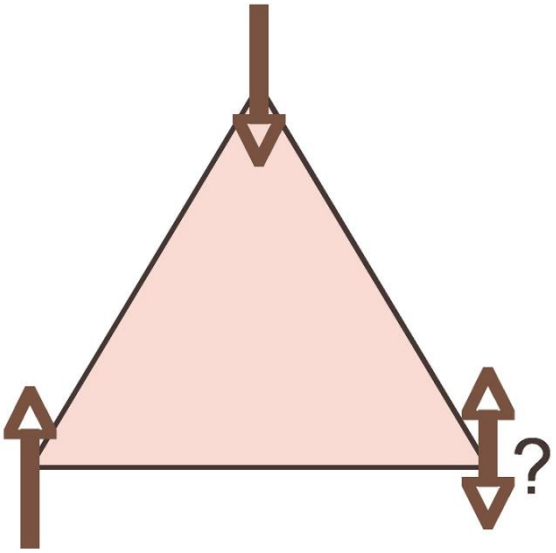

Figure 2. *Antiferromagnetic Ising spin triangular lattice.*

In each corner of the triangle, Ising spins point either up or down along the *z*-axis. The spins interact antiferromagnetically with each other to minimize the energy of the system. This means that a pair of spins will have the other spin up while the other is down. However, in a triangular system with three spins this is impossible: while two of the spins form an up/down pair, one spin always remains frustrated. The minimum energy will therefore be a degenerated state of several frustrated sub-states.

To solve this simple case of the Ising spin triangular lattice we need to determine a Hamiltonian H and diagonalize it to obtain the energy eigenvalues and eigenvectors. The Heisenberg spin Hamiltonian is written as

$$H = \sum_{ij} J_{ij} \boldsymbol{S}_i \cdot \boldsymbol{S}_j. \tag{2.2}$$

Here i,j are the spin indices and J_{ij} is the exchange constant matrix $\boldsymbol{J}$, and $\boldsymbol{S_{i,j}}$ are the spin operators in a vector form. To simulate antiferromagnetic coupling between nearest neighbor spins, the exchange constant will be zero when $i = j$ but $-J$ when i and j correspond to nearest neighbor spins. For an antiferromagnetic ground state $J < 0$ is selected,

while for a ferromagnetic ground state $J > 0$ is selected. In this example with three spins in a triangle the exchange constant matrix is

$$\boldsymbol{J} = -J\begin{bmatrix} 0 & 1 & 1 \\ 1 & 0 & 1 \\ 1 & 1 & 0 \end{bmatrix}. \tag{2.3}$$

Spin vectors $\boldsymbol{S_{i,j}}$ have *x*-, *y*-, and *z*-components. Ising spins have only values ±1/2 in the *z*-direction. The dot product for the spin vectors can be written as

$$\boldsymbol{S}_i \cdot \boldsymbol{S}_j = \boldsymbol{S}_{iz} \cdot \boldsymbol{S}_{jz} + \tfrac{1}{2}\left(\boldsymbol{S}_{i-} \cdot \boldsymbol{S}_{j+} + \boldsymbol{S}_{i+} \cdot \boldsymbol{S}_{j-}\right). \tag{2.4}$$

Here the dot product of spin operators along *z*-axis $\boldsymbol{S}_{iz} \cdot \boldsymbol{S}_{jz}$ gives ±1/4 for Ising spins depending on whether the spins are of the same sign or not. If the lowering $\boldsymbol{S}_-$ and raising operators $\boldsymbol{S}_+$ are able to lower and raise their dot product we get a value of one. For a system with *n* Ising spins the multiplicity for the number of basic states is 2^n. Thus, the wave function can be described as a vector of $2^n \times 1$, which in this example is given by

$$\psi = \begin{pmatrix} |\downarrow\downarrow\downarrow\rangle \\ |\uparrow\downarrow\downarrow\rangle \\ |\downarrow\uparrow\downarrow\rangle \\ |\uparrow\uparrow\downarrow\rangle \\ |\downarrow\downarrow\uparrow\rangle \\ |\uparrow\downarrow\uparrow\rangle \\ |\downarrow\uparrow\uparrow\rangle \\ |\uparrow\uparrow\uparrow\rangle \end{pmatrix}. \tag{2.5}$$

Operating the Hamiltonian with the wave function vector yields a $2^n \times 2^n$ matrix as a result. The Hamiltonian term $\boldsymbol{S}_{iz} \cdot \boldsymbol{S}_{jz}$ applies only to the diagonal terms of the matrix, while $\frac{1}{2}\left(\boldsymbol{S}_{i-} \cdot \boldsymbol{S}_{j+} + \boldsymbol{S}_{i+} \cdot \boldsymbol{S}_{j-}\right)$ applies only to some of the non-diagonal terms. The result of the operation is given by

$$H\psi = -J\begin{bmatrix} 3/2 & 0 & 0 & 0 & 0 & 0 & 0 & 0 \\ 0 & -1/2 & 1 & 0 & 1 & 0 & 0 & 0 \\ 0 & 1 & -1/2 & 0 & 1 & 0 & 0 & 0 \\ 0 & 0 & 0 & -1/2 & 0 & 1 & 1 & 0 \\ 0 & 1 & 1 & 0 & -1/2 & 0 & 0 & 0 \\ 0 & 0 & 0 & 1 & 0 & -1/2 & 1 & 0 \\ 0 & 0 & 0 & 1 & 0 & 1 & -1/2 & 0 \\ 0 & 0 & 0 & 0 & 0 & 0 & 0 & 3/2 \end{bmatrix}\psi. \tag{2.6}$$

When the matrix is diagonalized, for example with MATLAB [19], the resulting ground states are given as follows:

$$n_{01} = \tfrac{1}{\sqrt{26}}(+3|\uparrow\downarrow\downarrow\rangle + |\downarrow\uparrow\downarrow\rangle - 4|\downarrow\downarrow\uparrow\rangle),$$

$$n_{02} = \frac{1}{\sqrt{26}}(-3|\uparrow\uparrow\downarrow\rangle - |\uparrow\downarrow\uparrow\rangle + 4|\downarrow\uparrow\uparrow\rangle),$$

$$n_{03} = \frac{1}{\sqrt{78}}(-5|\uparrow\downarrow\downarrow\rangle + 7|\downarrow\uparrow\downarrow\rangle - 2|\downarrow\downarrow\uparrow\rangle),$$

$$n_{04} = \frac{1}{\sqrt{78}}(+5|\uparrow\uparrow\downarrow\rangle - 7|\uparrow\downarrow\uparrow\rangle + 2|\downarrow\uparrow\uparrow\rangle).$$

The first exited states are given by

$$n_{11} = \frac{1}{\sqrt{3}}(-|\uparrow\downarrow\downarrow\rangle - |\downarrow\uparrow\downarrow\rangle - |\downarrow\downarrow\uparrow\rangle),$$

$$n_{12} = \frac{1}{\sqrt{3}}(-|\uparrow\uparrow\downarrow\rangle - |\uparrow\downarrow\uparrow\rangle - |\downarrow\uparrow\uparrow\rangle),$$

$$n_{13} = |\downarrow\downarrow\downarrow\rangle,$$

$$n_{14} = |\uparrow\uparrow\uparrow\rangle.$$

The ground state can be interpreted to have a four-fold degeneracy which is half of the available eigenstates. For a larger-scale frustrated system the absolute ground state degeneracy would be even larger. This was proved by Wannier in 1950 [2] for an antiferromagnetic Ising triangular lattice.

2.4 Resonating valence bond (RVB) state

The resonating valence bond (RVB) state was first introduced by Anderson in 1973 [3]. It is a quantum spin liquid (QSL) state achieved by the mechanics of resonating valence bonds. This means that all possible valence bond couplings between spins are in a fluctuating superposition.

The ground state of an RVB state is highly degenerated and it is expected that there is no magnetic ordering down to zero Kelvin. An RVB state might emerge close to or at its ground state which requires certain conditions like a sufficiently low temperature. That is why the word “condensed” is sometimes used along RVB.

A valence bond solid (VBS) state is a sub-category of a valence bond state just like an RVB state. However, in contrast with RVB, in VBS pairs of spins are maximally entangled to each other forming a determined pattern of valence bonds in the lattice. This is also shown in Figure 3.

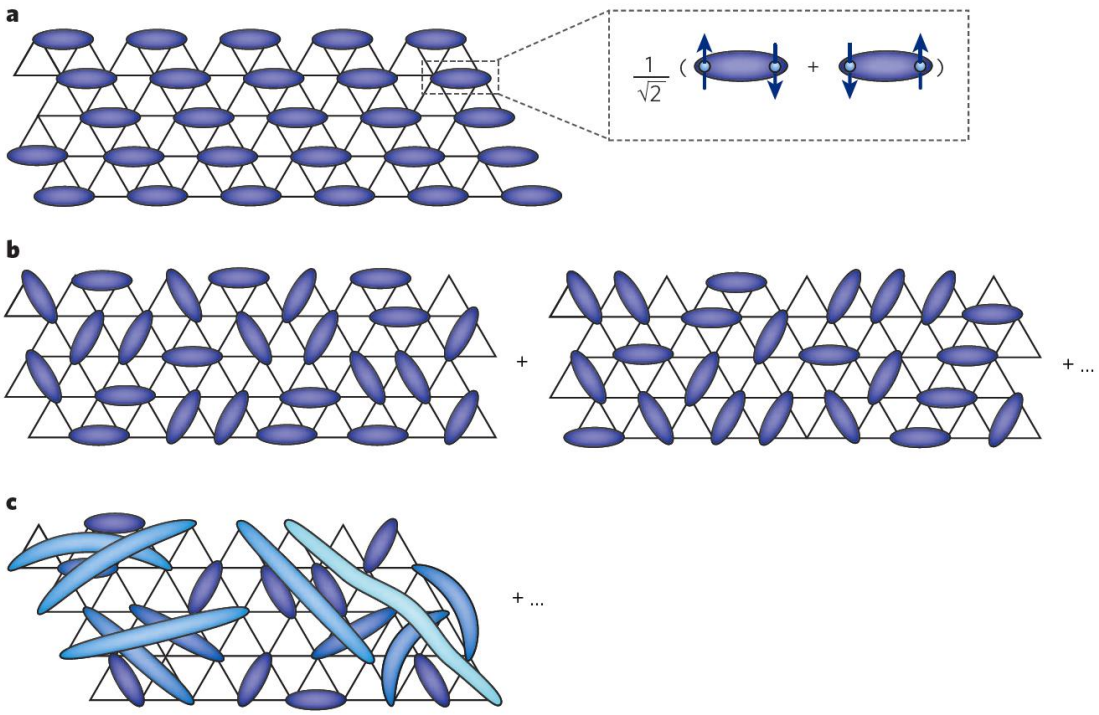

Figure 3. *Valence bond states of a frustrated antiferromagnet. Blue ovals represent valence bonds between two points on the lattice. (**a**) Valence bond solid (VBS) state. (**b**) Resonating valence bond (RVB) state with nearest-neighbor ordering. (**c**) Long-range ordered RVB state. Figure is taken from Ref. [1].*

In Figure 3 it is illustrated that a VBS state (**a**) is a static set of valence bonds while a RVB state (**b**, **c**) is a superposition of many sets of valence bond arrangements. The idea that an RVB state could also allow long range ordering (**c**) is presented. From the figure it can also be seen that a VBS state breaks the lattice symmetry by the definite pattern of localized valence bonds. This is not the case of the liquid-like RVB state, where the valence bonds are non-localized.

In 1983 Anderson [20] suggested that an RVB material, which is by default an insulator, could become a high-temperature superconductor with appropriate doping. This would make the spins already entangled in valence bonds act as Cooper pairs. Anderson's paper [20] raised a wide interest towards RVB materials and spin liquids in general. However, so far there is no conclusively sufficient experimental evidence of the existence of an RVB or QSL state.

2.5 Spinon excitations

The long-range valence bond ordering in an RVB state in Figure 3(**c**) offers a mechanism to create spinons, quasi-particles that carry spin quantum numbers. The longer the range of the spin coupling, the smaller the probability in the partition function, which also corresponds to the bond energy. This is illustrated by a lighter color in the longer bonds in Figure 3(**c**). Long-range valence bonds with low bonding energy break rela-

tively easily forming spinon excitations. All QSLs or RVBs are expected to have these spinons. Rearrangement of valence bonds in the lattice is another creation mechanism for spinon excitations, which does not require bond breakage nor long-range ordering. Some RVBs are also expected to produce spinons with exotic fractional quantum numbers, for example $S = 1/4$ [1].

Neutron scattering is probably the best tool to detect spinons in a QSL lattice. As a spin $S = 1/2$ particle without charge, a neutron is not distracted by electromagnetic interactions and ignore spin-neutral valence bonds. However, it will interact with spinon excitations. For each type of QSL, depending on the spinon emergence mechanism, there should be a distinct spinon dispersion relation. This could be observed with neutron scattering techniques giving evidence of the existence of a QSL. So far by using inelastic neutron scattering, spinon excitations have been measured for a frustrated one-dimensional lattice of spin $S = 1/2$ antiferromagnets [21].

3. COMPOUND $LIZN_2MO_3O_8$

The compound $LiZn_2Mo_3O_8$ is under investigation in this study. In this chapter some of its characteristics are presented. Previous work reported in the literature is also discussed. Finally, powder and single-crystal sample synthesis of $LiZn_2Mo_3O_8$ is explained.

3.1 $LiZn_2Mo_3O_8$ structure

The insulating $LiZn_2Mo_3O_8$ cluster antiferromagnet was first reported by Torardi in 1985 [22]. It has magnetic Mo_3O_{13} clusters that can be considered to be similar to that of cluster Mott insulators [23]. The electronic orbital structure of these Mo_3O_{13} clusters was presented by Sheckelton in 2012 [8]. The cluster has seven valence electrons, six of which are located in bonds between three molybdenum atoms. The remaining electron is unpaired and delocalized in a symmetric molecular orbital among the three atoms. This offers stability towards symmetry breakage that can disrupt frustration. The $S = 1/2$ magnetic moment per each Mo_3O_{13} cluster is expected to be in antiferromagnetic interaction with neighboring clusters, possibly forming an RVB state.

The $LiZn_2Mo_3O_8$ compound, besides being a cluster, has a two-dimensional layered structure shown in Figure 4. Mo_3O_{13} clusters are connected to each other by shared oxygen atoms forming planes in a triangular pattern. The cluster alignment is such that the molybdenum atoms can be considered to form an anisotropic Kagome lattice [14]. The Mo_3O_8 planes are separated by layers of Li^{1+} and Zn^{2+} ions which are located in partially occupied shared lattice positions shown in Figure 5. These ions supply Mo_3O_{13} clusters with electrons, which leads to magnetism. It is crucial that the occupations of Li and Zn are stoichiometric, so that each Mo_3O_{13} cluster receives an odd number of valence electrons for its $S = 1/2$ magnetic moment, and that frustration disrupting symmetry breakage will not happen.

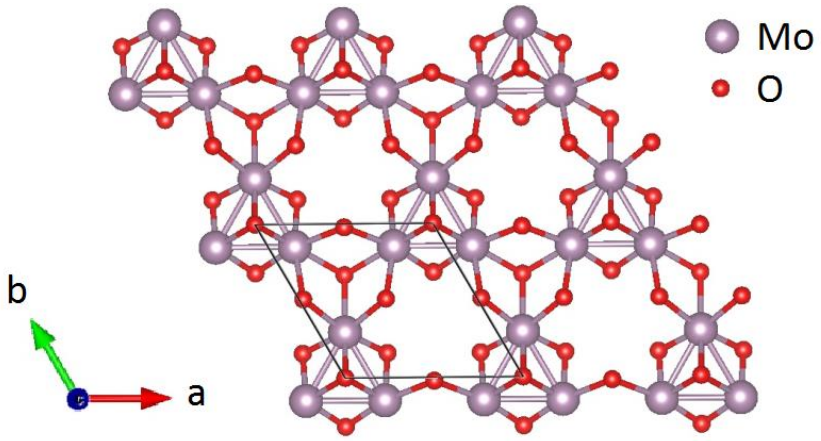

Figure 4. *Atomic structure of $LiZn_2Mo_3O_8$ viewed normal to Mo_3O_8-planes (see text).*

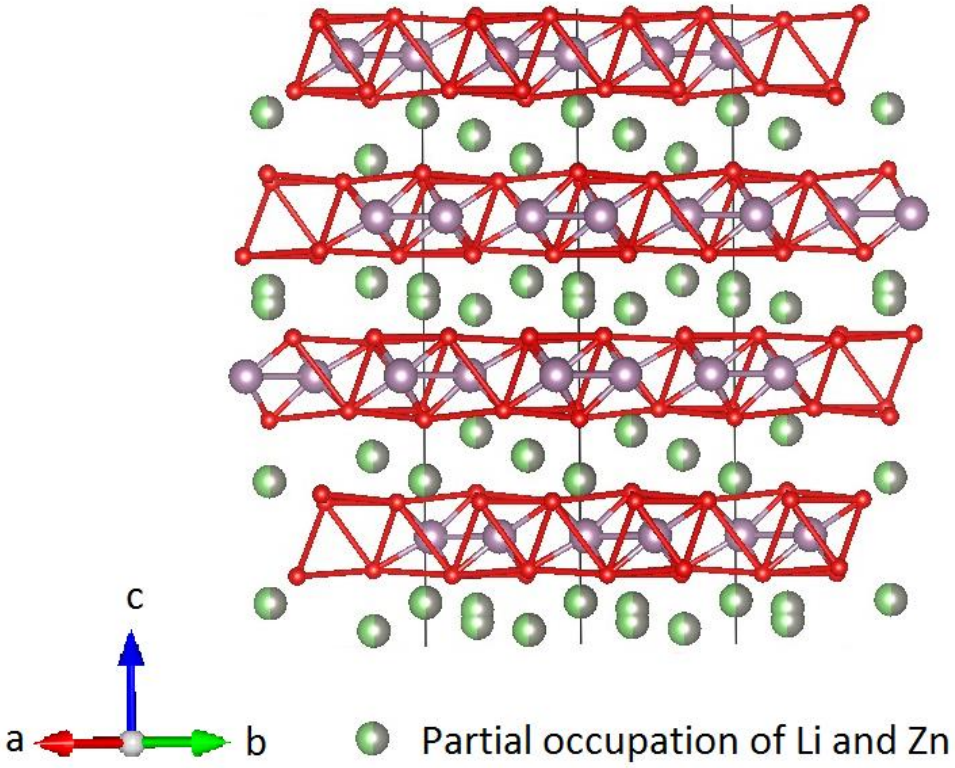

Figure 5. *$LiZn_2Mo_3O_8$ structure viewed perpendicular to Mo_3O_8-planes (see text).*

Both Figure 4 and Figure 5 were prepared with VESTA [24] software using crystallographic data from supplementary supporting information given in Ref. [12]. The lattice coordinates *a*, *b* and *c* relate to the corresponding lattice constants. The atoms are represented by green, grey, violet and red spheres indicating lithium, zinc, molybdenum and oxygen, respectively. As a ball-stick model the bonds between atoms are shown by lines colored as the atoms involved in the bonds. The unit cell is drawn with black lines. The lattice multiplicity is $Z = 6$ so the unit cell is shown entirely from the normal Mo_3O_8 plane view, while the perpendicular view shows only four out of six planes. The unit cell dimensions, in other words lattice constants, vary depending on source but they are

approximately $a = b = 5.8$ Å and $c = 31$ Å. The calculated density based on cell parameters is roughly 6.0 g cm^{-3}. The $LiZn_2Mo_3O_8$ compound has as space group $R\bar{3}m$ #166.

Another important compound for this work is $Zn_2Mo_3O_8$. It is non-magnetic so it can be used as a non-magnetic reference. Many samples presented in this work have a secondary phase of $Zn_2Mo_3O_8$. The compound lacks the lithium atom altogether but has otherwise similar atomic positions with a layered cluster-structure as $LiZn_2Mo_3O_8$. However, the lattice multiplicity is $Z = 2$ and the space group is $P6_3mc$ #186.

3.2 Previous studies on $LiZn_2Mo_3O_8$

The cluster antiferromagnet $LiZn_2Mo_3O_8$ has attracted interest since Sheckelton in 2012 [8] suggested that the compound might possibly hold a condensed resonating valence bond (RVB) state. In that paper with the support of orbital calculations it was pointed out that the spin magnetic moments $S = 1/2$ are delocalized among a cluster of three molybdenum atoms. This creates a stable basis for geometrical frustration to take place. Sheckelton also presented magnetic susceptibility data (Figure 6) of $LiZn_2Mo_3O_8$ with two Curie-Weiss temperature regions.

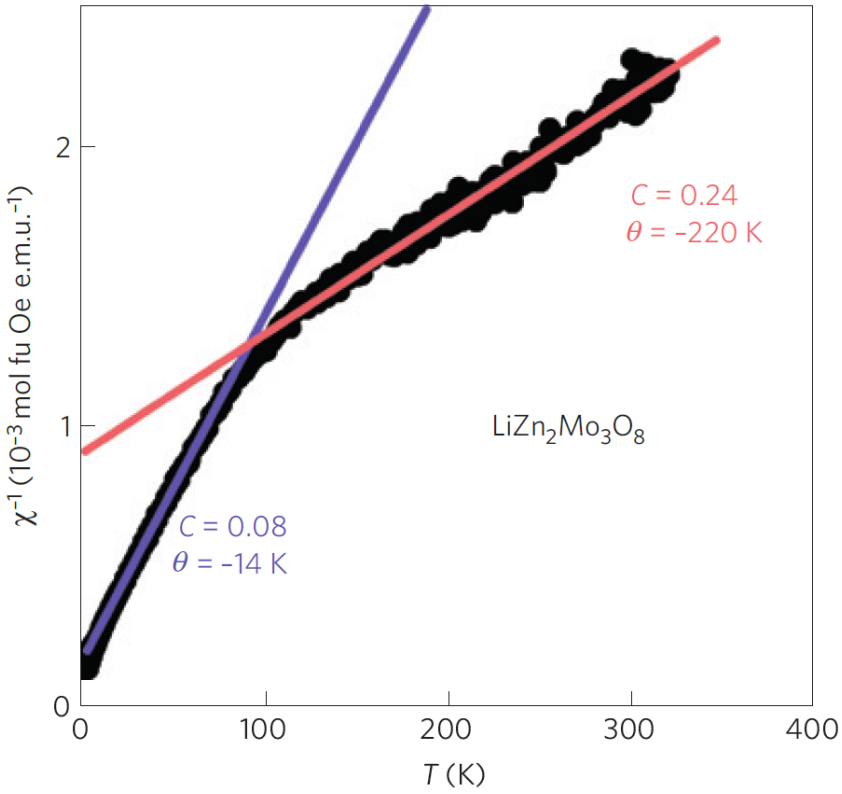

Figure 6. *Temperature dependent inverse magnetic susceptibility of $LiZn_2Mo_3O_8$. Figure from Ref. [8].*

Figure 6 is a temperature-dependent inverse magnetic susceptibility plot, where a linear Curie-Weiss fit is used to obtain Curie constants C and temperatures θ (or T_C in this

work). The plot suggests a 2/3 loss of the spin magnetic moment in the lower region (0–100 °C) with a Curie constant C = 0.08 compared to the upper region (100–300 °C) with C = 0.24. Similar temperature-dependent entropy and heat capacity datasets were also presented in the same source [8].

In 2013 Flint [9] explained the 2/3 disappearance of spins with a theory, where a third of the Mo_3O_{13} clusters turns clockwise and another third turns counterclockwise, while the last third remains the same. This changes the bond lengths in such a manner that the spins couple strongly together as a VBS state in a honeycomb pattern. This would leave only a third of the spins capable of forming a frustrated state.

In 2014 two experimental papers about the issue came out by Mourigal [10] and Sheckelton [11]. The first paper featured datasets from powder sample inelastic neutron scattering (INS). The latter work featured datasets from electron spin resonance (ESR), ^{7}Li nuclear magnetic resonance (NMR), and muon spin rotation (μSR) spectroscopies. The INS results confirm that at ≤ 30 K there are S = 1/2 excitations of energies in magnitude of nearest and next-nearest neighbor valence bonds involving Mo_3O_{13} clusters. However, the INS dataset differs from that expected of a triangular lattice Heisenberg S = 1/2 antiferromagnet with long-range order. In the other experimental paper 0, perhaps the most significant result was the ESR. Only one resonating peak was found, which heavily supports that magnetism in $LiZn_2Mo_3O_8$ arises from the S = 1/2 magnetic moments per cluster. Neither of these papers [10], 0 could exclusively prove or rule out the possibility for a spin liquid state in $LiZn_2Mo_3O_8$.

In 2015 Sheckelton published a paper [12], where the effect of doping S = 1/2 holes in molybdenum clusters was investigated. This was achieved in a controlled manner by a chemical method to remove Zn^{2+} ions from $LiZn_2Mo_3O_8$ samples. The hole doping did not seem to cause lattice symmetry distortion. The doping dependence on lattice constants and magnetic susceptibility were presented.

In 2015 Haraguchi [13] published datasets of two triangular lattice Mo_3 cluster (space group $P6_3mc$) antiferromagnets $Li_2InMo_3O_8$ and $Li_2ScMo_3O_8$. The first set shows magnetic ordering at ~12 K, while the latter did not order at low temperatures and thus it remains as a spin liquid candidate. Both compounds show, with only one Curie-Weiss temperature region, a more typical antiferromagnetic Curie-Weiss susceptibility behavior compared to $LiZn_2Mo_3O_8$, which shows two Curie-Weiss regions (Figure 6). It will be interesting to see if more experimental and theoretical papers will appear for the $Li_2ScMo_3O_8$ compound in near future.

In 2015 Chen [14] presented a theoretical model for $LiZn_2Mo_3O_8$ and similar compounds to calculate spin interactions. It is an anisotropic Kagome lattice with partial electron filling based on the Hubbard model.

3.3 $LiZn_2Mo_3O_8$ synthesis

In 1985 Torardi [22] presented two solid-state methods for the synthesis of $LiZn_2Mo_3O_8$. In the first method a ratio of 1:2:5 Li_2Mo_4, ZnO, and MoO_2 were ground, pelletized, and sealed in an evacuated molybdenum tube, which was also sealed in an evacuated quartz tube, and held at 1100 °C for two days. This produced black plate like crystals large enough for X-ray single-crystal diffraction to determine the crystal structure of the newly found compound. In this thesis the results of this method was successfully reproduced.

The second method used by Torardi was a stoichiometric ratio of Li_2MoO_4, ZnO, MoO_2, and Mo pelletized and reacted in a Molybdenum tube for five days at 1100 °C. After a wash of hydrochloride acid (HCl) this produced 90 % pure powder sample with traces of MoO_2 and Mo.

In 2012 Sheckelton presented an improved method for synthesizing a phase-pure powder sample of $LiZn_2Mo_3O_8$ [8]. Instead of a stoichiometric ratio, excess Li_2MoO_4 and ZnO would make sure all of the MoO_2 and Mo would react. Before mixing and grinding the ingredients together, Li_2MoO_4 and ZnO were dried overnight at 160 °C and MoO_2 purified under argon gas. The reactants were then pelletized and put into an alumina crucible which was evacuated and double-sealed in silica tubes. This reaction vessel was then reacted in a furnace by a heating sequence shown in Figure 7. To ensure a more perfect reaction, the product was then regrounded and heated in the same manner for a second time.

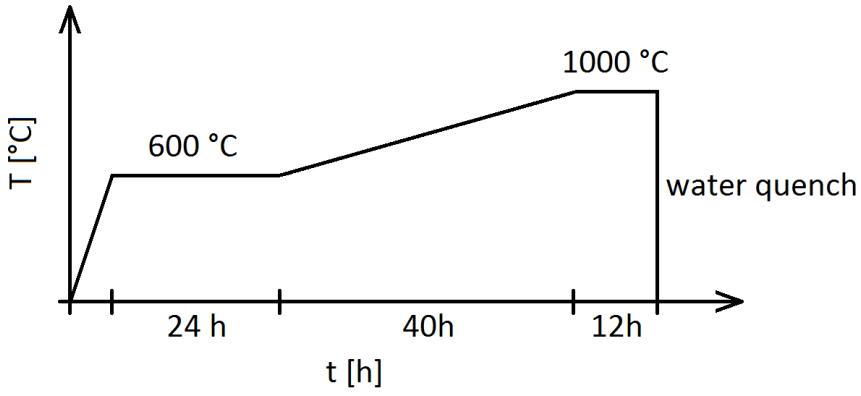

Figure 7. *Heating sequence for the solid-state reaction of $LiZn_2Mo_3O_8$.*

The heating sequence in Figure 7 is a set of time-dependent temperature steps. These instructions are programmed into the furnace. The first step heats the reaction vessel from room temperature to 600 °C. Sheckelton did not specify at which rate this was done, but in this thesis a ramp of six hours was used. The second step is at 600 °C for 24 hours. There was no explanation in Ref. [8] why this step is needed, but an educated guess is that at this point the ingredients start to produce vapor pressure, which could

break the reaction vessel without the relaxation period. The third step increases the temperature by a steady rate of 10 °C per hour. The reason for this slow rate is most probably to deal with the vapor pressure. Also solid-state reactions will most likely begin at some point when the temperature rises. The fourth step is the final temperature of 1000 °C for 12 hours. This is ended by quenching the reaction vessel into water. The rapid cooling of the product $LiZn_2Mo_3O_8$ would minimize its possible decomposition into some other compounds below 1000 °C. Figure 8 shows reacted pellets after the water quench and removal from the sample vessel.

Figure 8. *Pellets of 10 mm diameter after solid-state reaction.*

The powder sample synthesis used in this study is based on the method of Sheckelton [8] with some changes. MoO_2 was used as received, instead of purifying it under argon gas, because the supplier provided MoO_2 with 99.9% purity, and X-ray diffraction confirmed that there were no significant impurity peaks. A single silica tube was used instead of double tubes. Silica wool was used inside the tube to prevent the crucible breaking the tube due to thermal expansion. 0.25 atmosphere of argon gas was inserted in the vacuum. At 1000 °C the argon gas pressure was supposed to reach 1.0 atmosphere making the reaction vessel more durable when the silica glass would soften. The regrinding and re-reacting of the sample was omitted after the initial sample synthesis attempts, because the majority of the ingredients would react in the first heating and this was also confirmed by the X-ray measurement. However, the three-molar HCl wash was considered to be necessary to remove unreacted Li_2MoO_4 and ZnO. A sample size of 11 grams was usually used for powder samples.

3.3.1 Single-crystal growth

There are many techniques for growing single-crystals. In Quantum Spin Physics Laboratory at Tohoku University in Japan, where the thesis work was carried out, there are capabilities for many single-crystal growth methods with different kinds of furnaces

ranging from muzzle to image and arc furnaces. In this study only the solid-state method was tried and this method was a modification based on powder sample synthesis.

A few trials and errors of the powder crystal sample method used by Sheckelton [8] and the single-crystal method used by Torardi [22] were done. A succesful single-crystal growth of $LiZn_2Mo_3O_8$ was only achieved when the Torardis single-crystal recipe [21] was followed carefully. This included using a molybdenum crucible which was sealed by arch welding under a vacuum. However, a silica tube sealing was used instead of a quartz tube.

4. METHODS

This section explains the experimental methods used in this thesis work and in future studies. The methods include experimental data acquisition and analysis methods.

4.1 Powder X-ray diffraction and Rietveld analysis

Powder X-ray diffraction (XRD) is an important tool for example in inorganic chemistry, metallurgy and condensed matter physics. It is used for the determination of the crystal structure along lattice constants and atomic positions and other crystallographic data. In this thesis work, XRD allowed to perform atomic structure analysis of newly synthesized powder samples relatively inexpensively and quickly and to verify that these samples were of the intended compound. As such XRD was the most frequently used experimental method.

X-ray diffractometers acquire Bragg reflection peak pattern data with intensity as a function of the angle (2θ) of the reflection. Rietveld analysis is used to make a fit to this XRD peak pattern data, also called a powder pattern, by iteratively refining different parameters such as lattice constants, atomic positions, and peak shape factors. The weakness of the Rietveld analysis is the fact that it requires a good initial estimate of the target sample composition, crystal structure, and other parameters. The factors have to be first obtained individually by other means which can be time consuming. An example of powder pattern data and its Rietveld fit is shown in Figure 9.

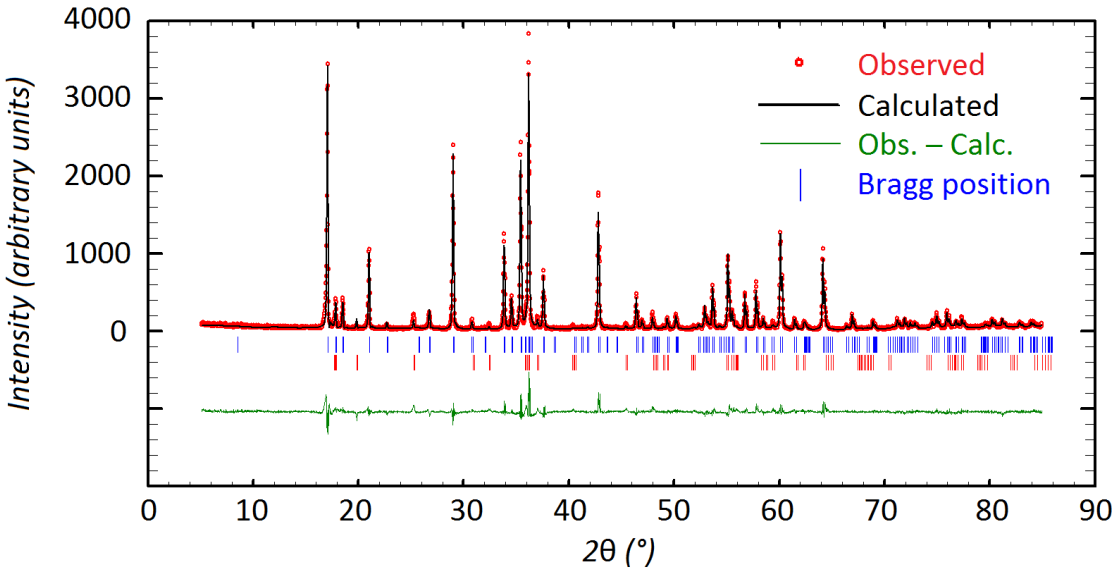

Figure 9. *Example of XRD data with Rietveld fit (see text). The sample is made with Type A $Li_{1-x}Zn_{2+x}Mo_3O_8$ recipe, x = 0.4.*

The Rietveld refinement fit is done to a powder pattern using Fullprof Suite Program (2.05) with the PCR-editor EdPCR (2.00) [25]. The vertical axis is the Bragg 2θ angle and the horizontal axis is the intensity. The red dots forming an almost continuous line are observed powder pattern data. The black line is a fit to the experimental data obtained by the Rietveld refinement. The green line is the difference between the observed and calculated data. The blue vertical lines are Bragg positions of the primary phase $LiZn_2Mo_3O_8$, and the red vertical lines are that of the secondary phase $Zn_2Mo_3O_8$.

All XRD measurements were done with Rigaku RINT-V X-ray diffractometer. The typical parameters used in this work were 2θ = 5–85°, step of recording the intensity data $2\theta_{step}$ = 0.02°, and scanning speed $2\theta_{speed}$ = 2°/min. Also slower speeds were used to get higher peak intensity data for Rietveld fits of better quality.

Usually XRD was performed right after a sample was made. By quickly checking the major peak positions it could be understood if the product was what it was supposed to be or not. Also possible impurity peaks could be seen. If an accurate Rietveld analysis was desired, the sample would be first meshed with a 50 micron mesh and then HCl washed and rinsed before performing the XRD. The mesh made the powder more homogenous in grain size, improving the statistic distribution of the powder pattern.

4.2 4-axis X-ray diffraction

4-axis or circle X-ray diffractometers are used especially for measuring single-crystal samples. The 4-axis refers to four different angles (2θ, ω, φ, χ) that can be controlled. These angles associated to the diffractometer are shown in Figure 10.

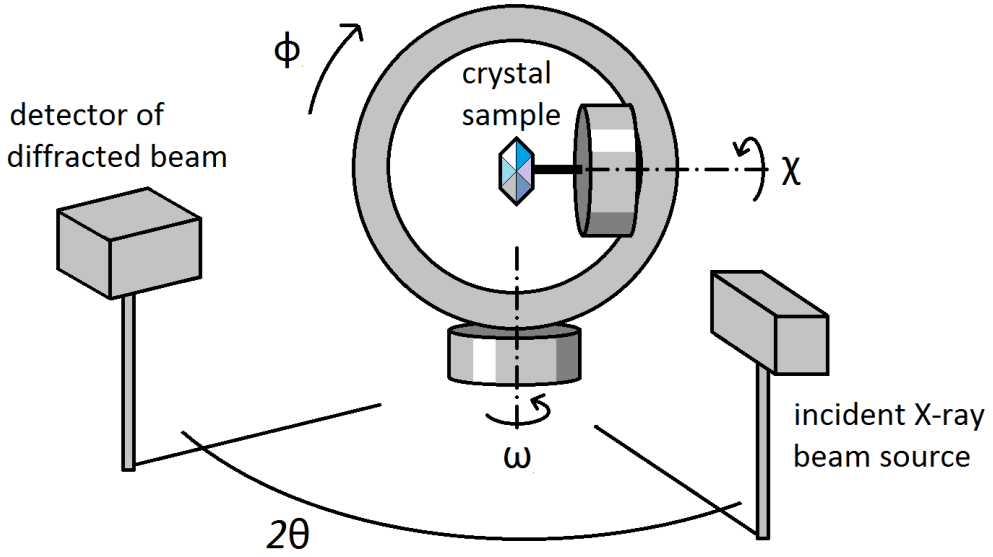

Figure 10. *Shematic figure of a 4-axis diffractometer.*

Angles 2θ and ω are the angles associates to Bragg reflection. Assuming that the X-ray source is stationary, rotating the detector around the crystal sample changes the 2θ angle. In order to get the correct Bragg reflections along 2θ, the ω angle has to be rotated according to a half of 2θ. Angles φ and χ are used to rotate the sample. Unlike powder crystal samples, which are considered to have crystals in all possible alignments according to the incident X-ray, single-crystal samples have to be rotated manually in all angular coordinates in order to be able to obtain all the Bragg reflections.

For this study, 4-axis diffraction is crucial to check the single-crystal composition and quality. Lattice constants can be determined more accurately than in XRD, which is useful, for example, to estimate the Li/Zn ratio in $LiZn_2Mo_3O_8$.

A conventional Copper or Molybdenum rotating target 4-axis X-ray diffractometer was used for measuring single-crystals and their quality. In this thesis target molybdenum K-α was used, which produces X-ray in wavelengths of 0.70930 and 0.71359 Å. A pyrolytic graphite monochromator was used to filter out background from the incident X-ray beam. In order to adjust the accuracy and peak intensity of the measurements, the width of the incident X-ray beam and the beam going to the detector could be controlled using a set of slits. In this thesis work the XRD source had always a pair of 1 mm slits, while the detector had either no slits at all, or a pair of 1 mm slits for course and fine measurements, respectively.

In a typical experiment a course φ–χ scan would be performed in the range of (0 0 6) direction to find the peak positions. Then a set of scans would be performed individually for each found peak to refine the peak coordinates (2θ, ω, φ, χ). Then peaks of a higher reciprocal lattice order would be found for the purpose of refining the 2θ and ω angles in order to be able to do accurate 2θ–ω scans in the corresponding peak direc-

tions. For example, for $LiZn_2Mo_3O_8$ the (0 0 6) reflection is in the c-axis direction and along that direction there is also (0 0 12), (0 0 18), and so on.

Before the single-crystal measurements, the crystals were picked up and glued on the top of a thin glass rod. These rods had been glued onto metal shafts that could be mounted on a goniometer. Using the goniometer, the single-crystal could be precisely aligned to the incident X-ray beam.

4.3 Magnetic property measurement system

Magnetic property measurement systems (MPMS) are high precision magnetometers based on a superconducting quantum interference device (SQUID) [26]. This superconducting loop with the quantum tunneling Josephson junction is sensitive to small changes in the magnetic field. The magnetometer of Quantum Spin Physics Laboratory was used in this thesis work. The device is MPMS-XL, a commercial model by Quantum Design which is shown in Figure 11.

Figure 11. *Magnetic property measurement system MPMS-XL.*

The MPMS system can measure fields as low as 10^{-7} electromagnetic units (emu) in the centimeter–gram–second (CGS) system. The lowest temperature is T = 1.9 K. The maximum DC magnetic field is H = 50000 Oersted (Oe). AC magnetization, electrical resistance, and a variety of other physical properties can also be measured. Typically, before the experiment the powder sample is weighted and loaded into a plastic capsule which in turn is mounted inside a plastic straw. This sample container is then put inside the vacuum pumped liquid nitrogen and helium cooled cryogenic sample chamber of the MPMS system. A high magnetic field is applied using superconducting coils. The response signal from the sample is detected by the SQUID circuit.

The MPMS system has its own control unit with a computer interface. All functions, such as heating and cooling the superconducting magnet and setting its field to a certain value, the temperature and vacuum control of the sample chamber, and the measurement process, can be controlled automatically and programmed to a measurement sequence.

In this study for powder samples MPMS was typically used to measure the magnetization in a range of 1.9–300 Kelvin in 10000 Oe magnetic field. The obtained magnetization data was analyzed to see what type of magnetic behavior occurs in the sample, and to estimate the occupation of spin magnetic moments per unit cell. To subtract the diamagnetic contributions from the measurement, the data of an empty sample was used. Also the diamagnetic contribution for the sample itself was roughly estimated to be $-2.0 \cdot 10^{-4}$ emu. As done in Ref. [8], an inverse magnetic susceptibility plot and a Curie-Weiss fit was performed to the data as shown in Figure 12.

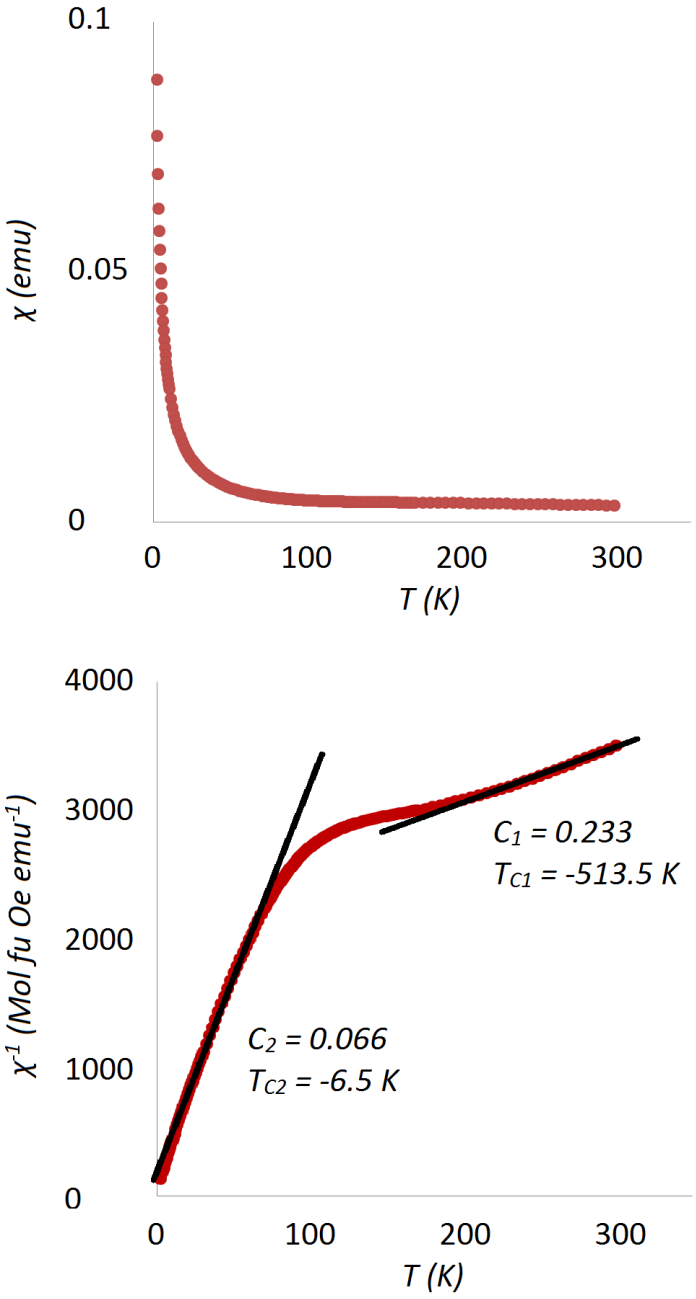

Figure 12. *Up: Temperature-dependent magnetic susceptibility under 10000 Oe for Type B* $Li_{1-x}Zn_{2+x}Mo_3O_8$*, x = 0.5 recipe sample. Down: Inverse susceptibility of the same data with two Curie-Weiss fits.*

In Figure 12 the (inverse) susceptibility in shown in the top (bottom) graph. The electromagnetic CGS units are used. The susceptibility has diamagnetic contributions subtracted as previously mentioned. The inverse susceptibility is scaled for the number of formula unit moles in the measured sample and the external magnetic field in Oe. To the inverse susceptibility Curie-Weiss fits are made in the linear regions. The slope determines the value of the Curie constant, while the Curie temperature is the point where the fit reaches zero. The Curie constant C_1 and Curie temperature T_{C1} are for the Curie-Weiss fit upper temperature range of 200–300 °C, while C_2 and T_{C2} are for the range of

10–70 °C. In this work the Curie constants are used for determine the amount of unpaired spin 1/2 magnetic moments in the samples.

The problem with the inverse susceptibility method for the Curie-value determination is the diamagnetic contribution χ_0. Diamagnetism is difficult to isolate from other forms of magnetism and therefore hard to conclusively determine for a given material both theoretically and experimentally. Depending on how one defines χ_0 will affect the Curie constant and temperature. A popular way to determine χ_0 is to adjust it until the inverse susceptibility curve becomes as linear as possible. Another way is to make an educated guess of χ_0 based on the atomic composition of the measured sample or some other available data.

4.4 Neutron scattering

Neutron scattering is an interesting tool used in condensed matter physics and in other fields. Neutrons with qualities such as zero charge and good penetration capability offer a range of unique possibilities in comparison to the more conventional experimental methods such as the X-ray scattering. Unfortunately, neutron scattering beam time is expensive and limited. There are only a handful of neutron source reactors available for experimental use around the world.

In Quantum Spin Physics Laboratory there is substantial experience of neutron scattering and good relations to neutron scattering facilities. Therefore, it has been planned from the beginning of this study to apply for neutron beam time if good quality samples with the promise of novel results are made. During this thesis work neutron scattering was performed on several samples, but these results will be reported later [15] with the exception of preliminary results outside the actual beam time.

There are two subclasses of neutron scattering: elastic neutron diffraction and inelastic neutron scattering. The former is used especially in soft matter physics for structure analysis just like X-ray diffraction, but also for the determination of three-dimensional magnetic structure. The latter is used to measure different kinds of lattice vibrations and excitations. A representation of the layout of a triple-axis neutron scattering device is shown in Figure 13.

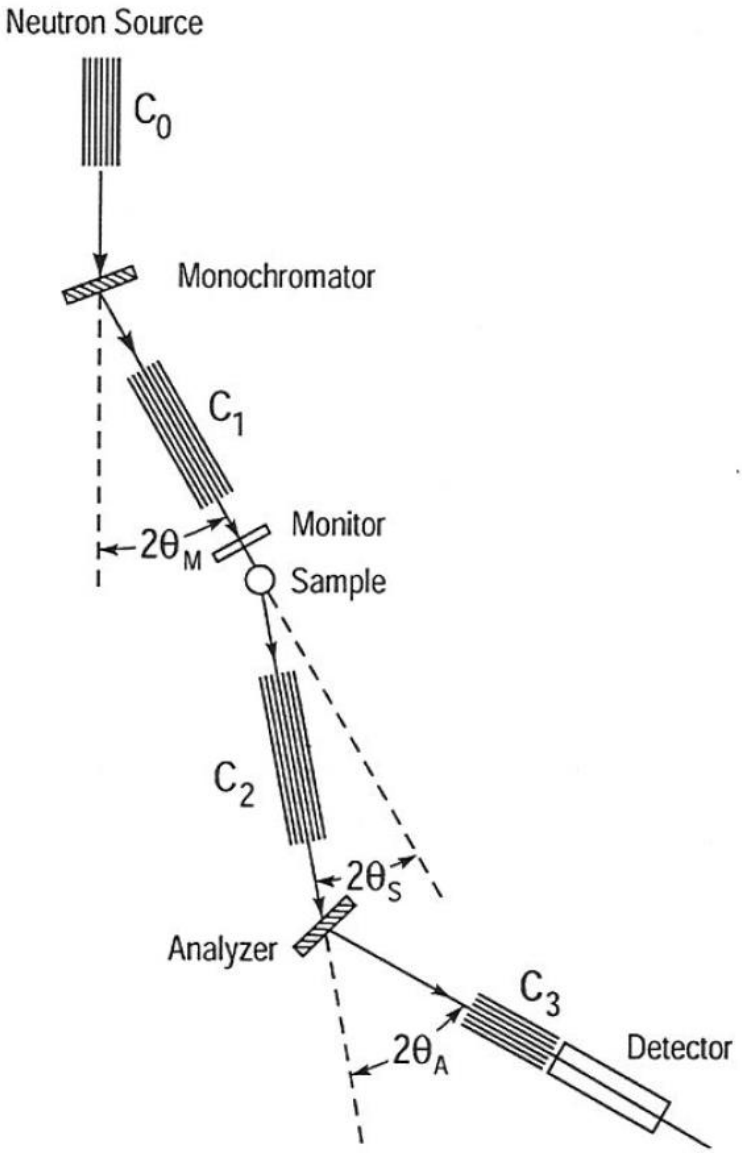

Figure 13. *Schematics of triple-axis neutron scattering apparatus. Figure is taken from Ref. [27].*

Figure 13 illustrates the principle of neutron scattering. Neutrons are generated with a neutron source C_0 which is usually a nuclear reaction. A monochromator crystal is used to select neutrons with a desired kinetic energy based on the Bragg reflection angle. *Cj* with j = 1–3 are collimators that help to focus the neutron beam. The analyzer is also a crystal that utilizes the Bragg reflection and it determines the energy of outgoing neutrons. The detector counts the number of neutrons that hit it. The monochromator and the analyzer could also be based on a time-of-flight technique. In that case it would not be called as a triple-axis apparatus.

4.4.1 Elastic neutron diffraction

From the point of view of nuclear physics, a neutron has no charge so it will not interact with the electron cloud but with the nucleus. The probability of the interaction is de-

pending on the target nucleus neutron cross section which tends to be large for light nuclei such as lithium and hydrogen, which are not easily detected by X-ray. On the other hand, many heavier metallic nuclei are almost transparent to neutrons. Combining X-ray and elastic neutron scattering, structures of broad range of atomic sizes can be measured.

For this study neutron powder diffraction (NPD) is useful for obtaining atomic positions and the occupation of lithium. Within the scope of this thesis work, only one sample of $LiZn_2Mo_3O_8$ was measured with NPD. This was a preliminary measurement outside of the awarded beam time at Australian Nuclear Science and Technology Organisation (ANSTO) with the neutron source OPAL research reactor and ECHIDNA high resolution powder diffractometer.

The Combined XRD + NPD Rietveld analysis was performed using the GSAS program [28] with EXPGUI interface (revision 1251) [29] (shown in Figure 14) to determine the crystal structure, lattice constants, second phase amounts, and Li and Zn occupations.

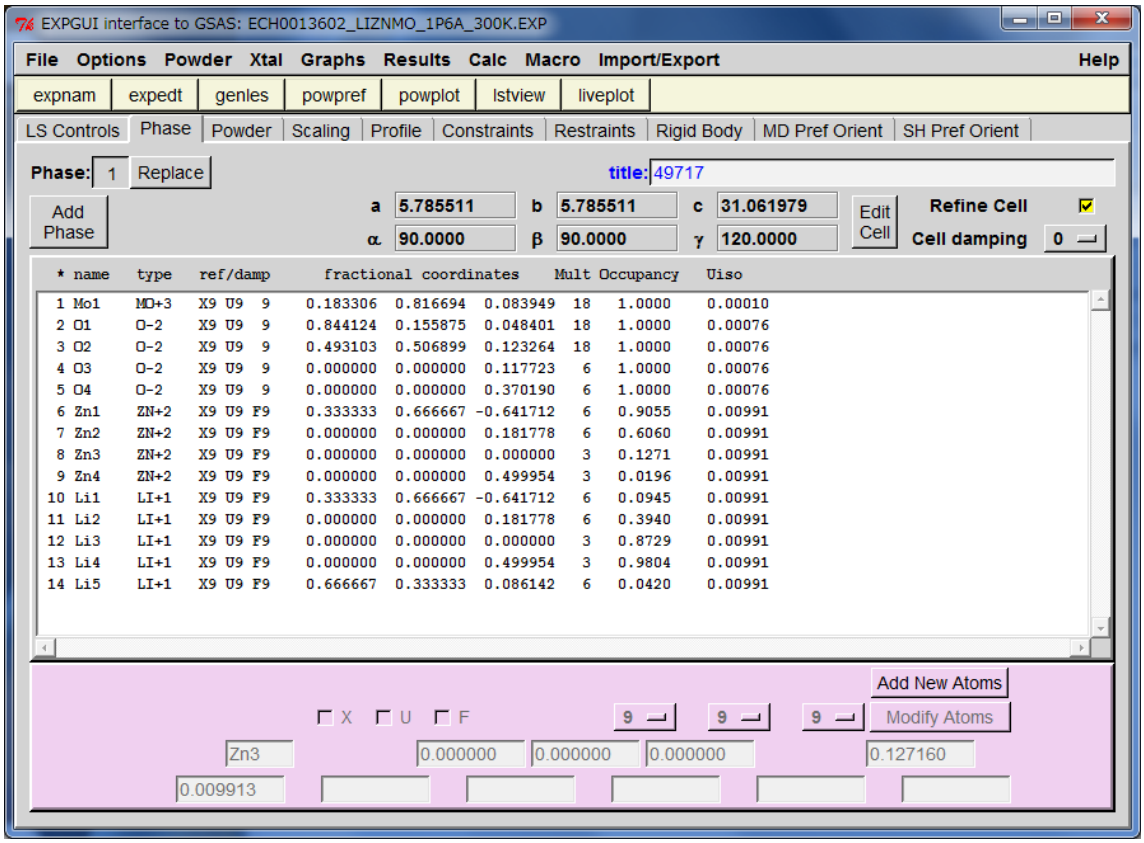

Figure 14. *Graphical user interface EXPGUI for general structure analysis system GSAS.*

In Figure 14 the EXPGUI interface shows the Phase tab open where the atomic structure parameters are presented. The lattice constants and angles associated to them are shown above the table. The columns from left to right are (i) the name of the atomic position in the unit cell, (ii) the atomic or ion element type, (iii) markers for which pa-

rameters are to be refined or left as they are, (iv) fractional coordinates along lattice axes, (v) multiplicity, (vi) occupancy, and (vii) the atomic displacement parameter.

4.4.2 Inelastic neutron scattering

As a fermion the neutron is a spin 1/2 particle and this makes it able to interact with unpaired spin 1/2 magnetic moments. This is used in inelastic neutron scattering to detect atomic vibrations and spinon excitations.

In the study of $LiZn_2Mo_3O_8$ possible resonating valence bond state inelastic neutron scattering could be used to detect spinon excitations. This would require a sufficiently large, good quality single-crystal. In recent studies [10] inelastic neutron scattering was done on a powder sample of $LiZn_2Mo_3O_8$, but this experiment could not yield definite evidence for RVB state.

4.5 Inductively coupled plasma mass spectrometry

Inductively coupled plasma (ICP) mass spectrometry is a highly sensitive device to measure atomic concentrations of material samples. For this work ICP mass spectroscopy would be a potential method to determine the Li/Zn ratio in LiZn2Mo3O8 samples more reliably than with combined XRD + NPD Rietveld analysis. However, this was left for future studies beyond the thesis work.

The downside for this ICP method is the fact that it destroys the samples in the process, but for relatively abundant powder samples this is not a problem. Measuring single-crystals with ICP is more challenging. A large amount of single-crystals would be needed for one ICP mass spectroscopy measurement.

5. RESULTS

This section is divided into six parts. The first part describes the initial attempts to reproduce the $LiZn_2Mo_3O_8$ powder sample as in Ref. [8]. This part presents also experiments performed on the successful reproduction sample and compares it to other $LiZn_2Mo_3O_8$ samples found in the literature. The second and third part explain recipes, Type A and Type B, to obtain powder samples of $LiZn_2Mo_3O_8$ with varying Li and Zn occupations. The fourth part presents the reproduction of the nonmagnetic $Zn_2Mo_3O_8$ powder sample. The fifth part is a summary of all $LiZn_2Mo_3O_8$ samples within the scope of this thesis work. The last part deals with the single-crystal study.

5.1 $LiZn_2Mo_3O_8$ reference sample

We made four attempts to reproduce the sample $LiZn_2Mo_3O_8$ with the method of Sheckelton [8]. After the reaction heating of the first trial, the X-ray pattern suggested that the right compound had been synthesized. The reaction heating was reperformed, which after the reaction vessel was broken in the water quench. Only a part of the sample was saved. A susceptibility measurement with MPMS was made on this sample. The shapes of the inverse susceptibility curves were similar, but the obtained Curie constants were smaller than in the reference.

The XRD data of the first sample looked good but not reassuring enough, so a second trial was started. The second sample was unsuccessful as the silica tube probably leaked in heating. There were dark grey and light brown components in the final reacted product. XRD of the products were taken, but no further studies were made. A preparation of the third sample was started, but the water quench was unsuccessful as the silica tube broke immediately when it hit the water. Only a small portion of the sample was saved, but the XRD data was the same as in the first sample.

For the fourth trial the water quench was improved. Instead of simply dropping the reaction vessel into the water as previously done, it was slowly inserted into the water to exclude mechanical shock. This turned out to be successful as the first and second reaction heating ended with the silica tube intact. When comparing the XRD patterns after both reactions, no significant differences between them were found. Therefore, the second solid state reaction was decided not to be done in future sample synthesis. This fourth successful reproduction attempt of Sheckelton's recipe [8] will be referred to as the *reference $LiZn_2Mo_3O_8$ sample*.

5.1.1 Structure and composition

To obtain good data for Rietveld analysis, the reference $LiZn_2Mo_3O_8$ sample was washed in HCl and the deposition method was used to filter out a suitable grain size instead of using a mesh. Then, a standard XRD measurement was taken of the sample which would be used together with NPD data for combined NPD + XRD Rietveld analysis. The Rietveld plot of the HCl washed grain size depose filtered XRD data is shown in Figure 15.

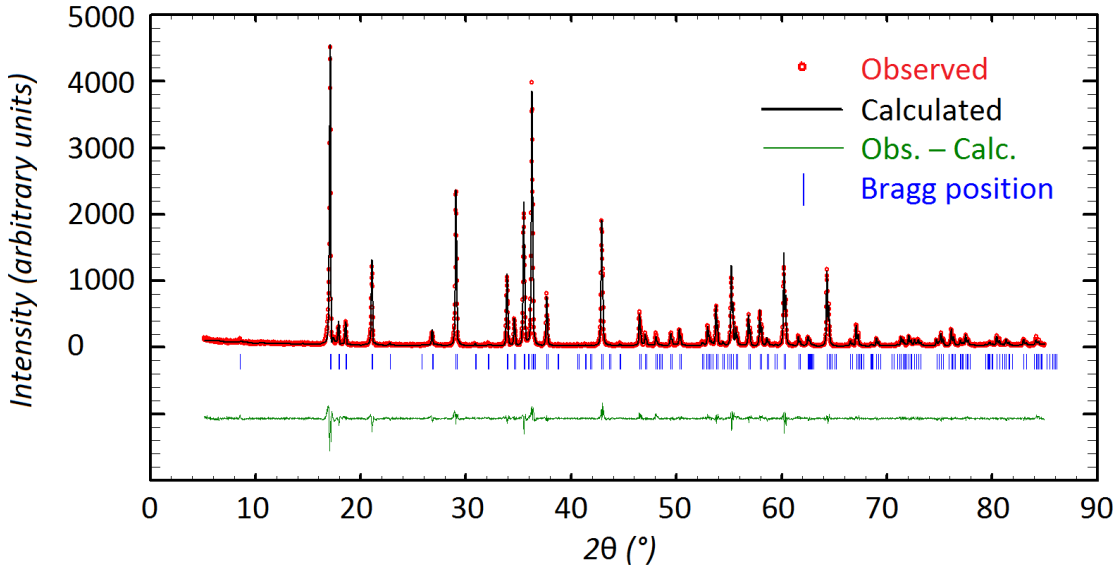

Figure 15. *Rietveld fit of the fourth sample LiZn2Mo3O8 used as the reference.*

The red marks show the experimental XRD data, the black line is the Rietveld fit, the blue vertical lines correspond to the Bragg position, and the green line is the difference of the observed and calculated data. The Rietveld fit was good on the average with R-factor = 10.7 and χ^2 = 2.27. The lattice constants *a* and *b* were 5.78551(9) Å and *c* was 31.0620(6) Å.

The reference $LiZn_2Mo_3O_8$ sample was sent to the Australian Nuclear Science and Technology Organisation (ANSTO) for preliminary NPD measurements. This was done using the neutron source OPAL research reactor together with the ECHIDNA high resolution powder diffractometer. Four datasets were measured: under temperatures of 3 K, 100 K and 300 K with incident neutron wave length λ = 2.4395 Å, and 300 K with λ = 1.6215 Å. The longer wavelength had higher intensity but less diffraction peaks than the shorter wavelength.

A combined XRD + NPD Rietveld analysis was performed with to the 300 K, λ = 1.6215 Å data using atomic positions given in Ref. [12]. An unrestrained analysis showed an occupation of 1.6/1.6 for Li/Zn. Restrains were added to limit the total occupancy of lithium and zinc shared sites to one yielding Li/Zn = 1.46(3)/1.58(1). The combined Rietveld fit is presented in Figure 16.

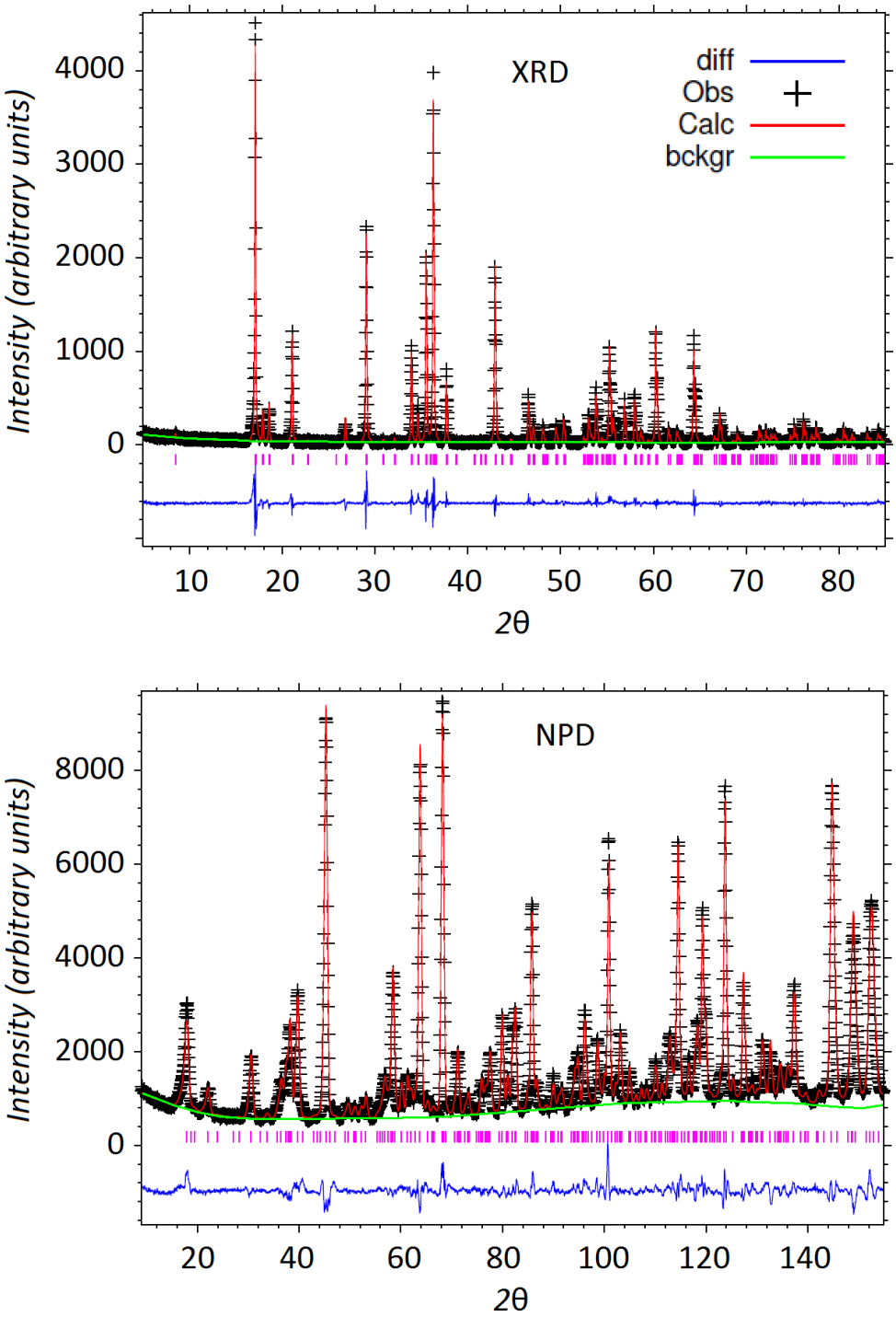

Figure 16. *Combined Rietveld fit of NPD and XRD data.*

In Figure 16 the upper graph shows the XRD data, while the lower graph shows the NPD data. Both show the powder pattern as intensity peaks along 2θ-axis. The observed data points are represented by black crosses, the Rietveld fit is a red line, the difference between observed and calculated data is shown as a blue line, the background subtraction is a green line, and Bragg reflection positions are pink vertical lines.

The 3 K, 100 K, and 300 K data with λ = 2.4395 were compared directly to each other. The datasets are presented in Figure 17.

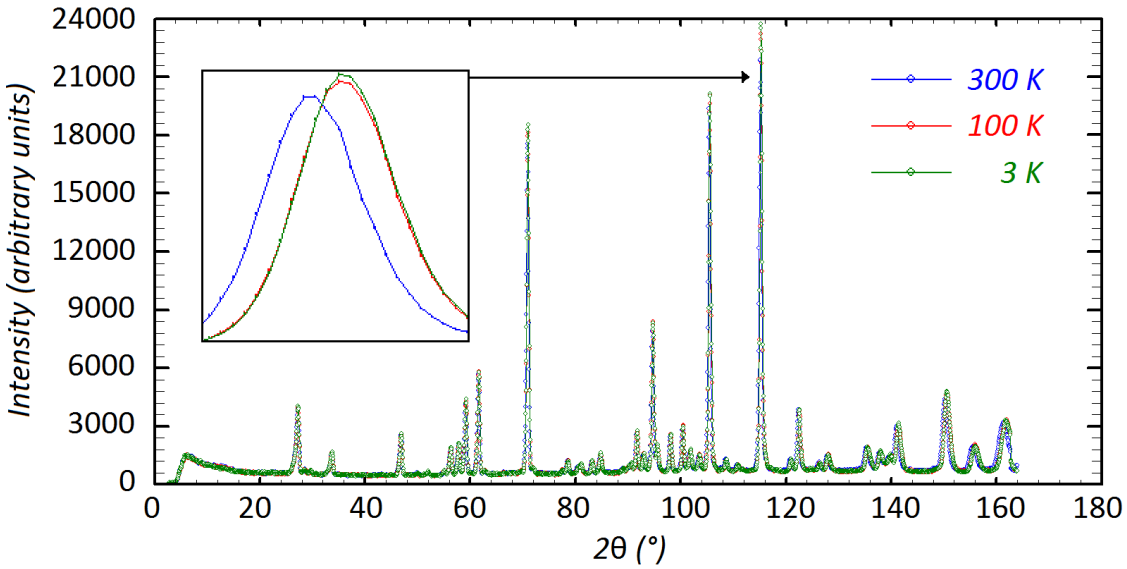

Figure 17. *Temperature-dependent NPD with λ = 2.4395.*

Due to thermal expansion the 100 K and 300 K peaks have slightly different positions and intensities. However, 3 K and 100 K results are almost the same. Otherwise all three datasets are quite similar, so they do not suggest any phase transitions in this temperature range. Based on these three datasets an analysis of the movement of lithium was performed. The combined NPD + XRD data obtained with GSAS were used in Fullprof Rietveld analysis to study the movement of lithium. Comparing to 300 K, the first Zn1/Li1 site moves 0.03 Å (0.04 Å), the second Zn2/Li2 site moves 0.09 Å (0.10 Å), and the fifth Li5 site moves 0.2 Å (0.9 Å) at 100K (3K).

The preliminary NPD of the reference sample of $LiZn_2Mo_3O_8$ was very useful for planning the scheduled beam time with the ANSTO ECHIDNA apparatus. The temperature-dependent datasets did not suggest any interesting phase transitions at 3 K and 100 K. A wavelength of 2.4395 Å was decided to be used in the actual ECHIDNA NPD beam time as it provides a higher intensity. This allows more samples to be measured than with the wavelength of 1.6215 Å.

A scanning electron microscope (SEM) scan of reference $LiZn_2Mo_3O_8$ was performed. Thirteen points were measured for O, Zn and Mo atomic percentages. Different surfaces of the crystals would give different percentages, so the total standard deviation of the all the data points is large. When fixing the atomic ratio of Mo/O to 3/8 the zinc concentration could be estimated to be 1.4(3), which is consistent with the NPD + XRD Rietveld analysis. Lithium concentration could not be reliably measured with SEM. No further SEM measurements were done in this study. A SEM picture of the $LiZn_2Mo_3O_8$ powder crystal sample is shown in Figure 18.

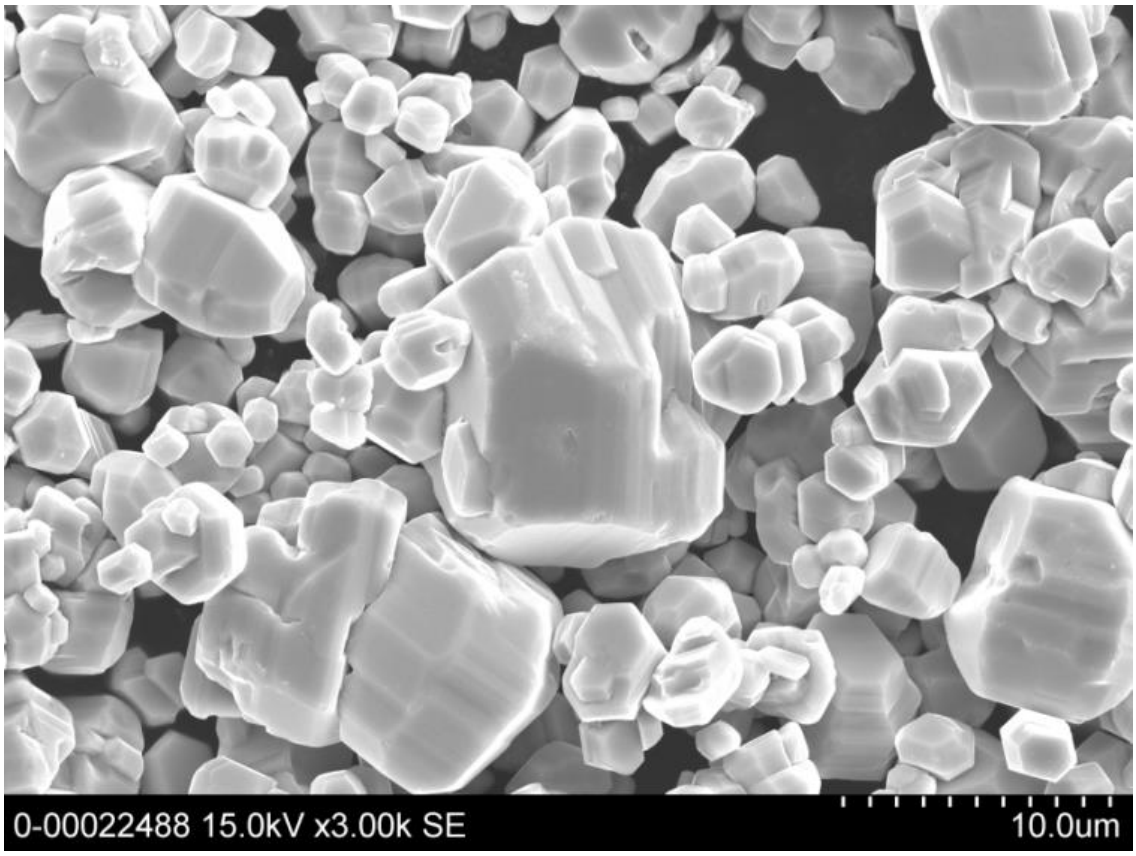

Figure 18. *Scanning electron microscope picture of reference $LiZn_2Mo_3O_8$ powder crystal sample.*

In Figure 18 we can see 10–100 μm sized crystals from the reference $LiZn_2Mo_3O_8$ sample. The crystals have a hexagonal shape, which is a consequence of the shape of the unit cell.

5.1.2 Magnetic behavior

Two susceptibility measurements with the MPMS were done to the reference $LiZn_2Mo_3O_8$ sample before and after the HCl wash. The obtained Curie constants were C_1 = 0.138 (0.146) and C_2 = 0.070 (0.073) for the HCl washed (unwashed) sample. The washable impurities had clearly some effect on the magnetic properties, and from this point on all powder samples were HCl washed before the MPMS measurement. The equivalent Curie constants given in Ref. [8] are C_1 = 0.24 and C_2 = 0.08. The HCl washed dataset is presented in Figure 19.

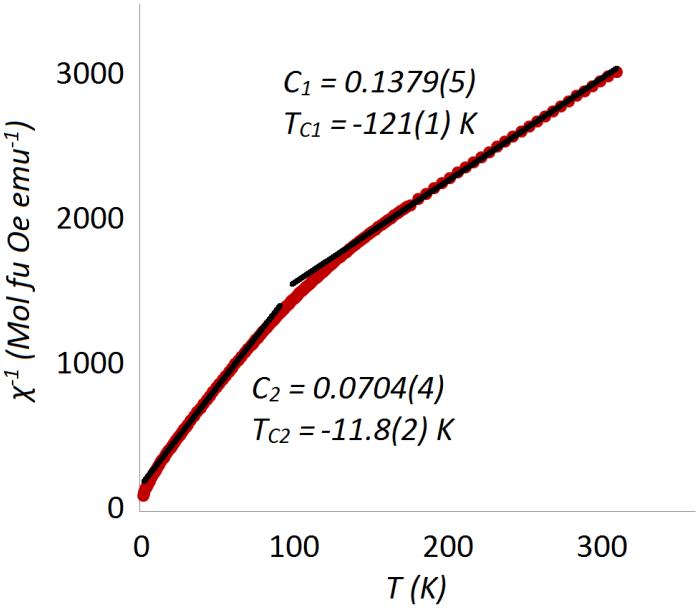

Figure 19. *Inverse susceptibility of the HCl washed reference LiZn2Mo3O8 powder sample.*

The susceptibility dependence on the magnetic field was measured for the unwashed reference $LiZn_2Mo_3O_8$ sample. This was done under temperatures of 1.9 K, 70 K, and 130 K for a range of magnetic fields of 0–50 000 Oe. In this dataset also the magnetic hysteresis was determined under 1.9 K by measuring the magnetization in an increasing and decreasing field order. The results are presented in Figure 20, which is called as a magnetization/magnetic field (M/H) curve.

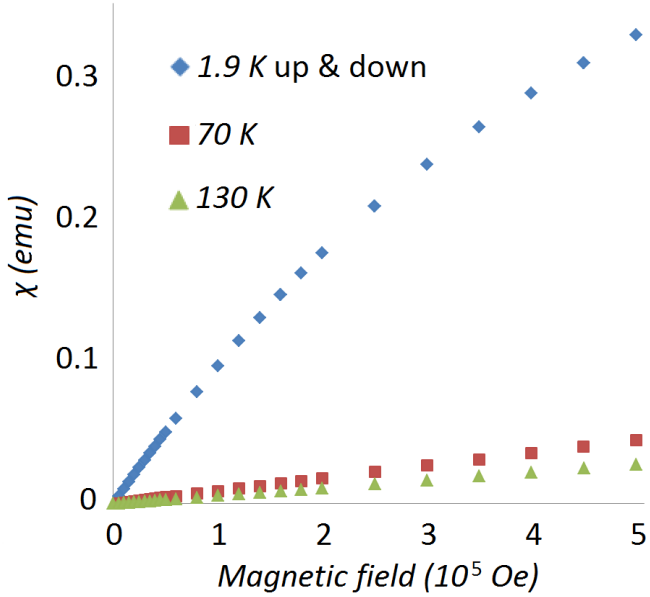

Figure 20. *M/H curve of the unwashed reference sample.*

In Figure 20 the x-axis is the magnetic field and the y-axis the magnetization in magnetic units (emu). The blue points show the data for 1.9 K, the red for 70 K and the green for 130 K. The 1.9 K data set contains points for both the increasing and decreasing field, but they are almost the same. The conclusion is that the effect of magnetic hyste-

resis is nonexistent. If a rough Brilloun function analysis is considered, where the data set is divided by the associate temperature, it looks as the 70 K and 130 K datasets are the same, but the 1.9 K result remains different. In this case, the conclusion could be that the M/H curves for 70 K and 130 K correspond to a different quantum number *S* from the 1.9 K curve. This is consistent with magnetization measurements, where below 70 K a different Curie-Weiss fit was observed compared to the higher temperature region.

5.1.3 Comparison to literature

Li/Zn ratios, lattice constants, and Curie constants C_1 of reference $LiZn_2Mo_3O_8$ samples are presented in Table 1.

Table 1. *Lattice constants and the Curie constants C_1 for the $LiZn_2Mo_3O_8$ samples from the literature compared with this work (reference $LiZn_2Mo_3O_8$ sample).*

Sample $LiZn_2Mo_3O_8$	**Li/Zn**	**a (Å)**	**c (Å)**	**C_1**
This work	1.46(3)/1.58(1)	5.78551(9)	31.0620(6)	0.1379(6)
Ref. [22] (1985)	Zn/Li ratio 2.0	5.8116(6)	31.013(8)	-
Ref. [8] (2012)	1.2(1)/1.8(1)	5.7956(1)	31.039(3)	0.24
Ref. [12] (2015)	1.0(1)/1.8(1)	5.80163(3)	31.0738(2)	0.375

The lattice constants in Ref. [22] were measured using a single-crystal. The Li/Zn ratio was determined by elemental analysis using a mixed phase product. Magnetic measurements were performed only in room temperature.

In Ref. [8] a combined XRD + NPD Rietveld analysis was performed. The magnetic susceptibility was obtained by subtracting the diamagnetic contributions χ_0 of an equimolar amount of non-magnetic $Zn_2Mo_3O_8$.

In Ref. [12] a chemical method was used to make zinc hole doped samples for the whole range of Mo_3O_{13} cluster electron occupancy of 0–1. A combined SXRD/Neutron diffraction was used for the Rietveld analysis for the native undoped sample. There was no explanation how the C_1 was obtained for the native sample. Apparently, the susceptibility was fitted by adjusting χ_0, so that the native C_1 became the ideal value of 0.375, which means full spin occupancy. The same χ_0 would then be used for the doped samples to get an idea how much spin occupancy is lost due to Zn hole doping.

It is difficult to make a unique comparison to the samples listed in Table 1 due to different methods used in different sources. However, some conclusions can be drawn. The reference $LiZn_2Mo_3O_8$ seems to be the worst in terms of an ideal Li and Zn occupation. Also the lattice constant *a* is the smallest among the listed samples. This could be explained by Vegard's law stating that atomic occupancies should also affect lattice con-

stants. C_1 in the reference $LiZn_2Mo_3O_8$ is also the furthest away from the ideal 0.375 value. This can be seen as a consequence of a fractional number of odd electrons per Mo_3O_{13} cluster donated by the Li^{1+} and Zn^{2+} ions.

The lattice constants by Torardi in 1985 [22] are the only values determined using a single-crystal. The elemental analysis resulting in a Zn/Li ratio of 2.0 cannot prove that the measured single-crystal has a perfect Li and Zn occupancy. However, this sample has the largest lattice constant *a*.

The group of Sheckelton seems to have improved their samples between 2012 and 2015. However, the most recent sample seems not to be perfect regarding the Li and Zn occupation.

5.2 Type A $LiZn_2Mo_3O_8$ recipe

The target formula for the Type A $LiZn_2Mo_3O_8$ recipe is

$$Li_{1-x}Zn_{2+x}Mo_3O_8 + 0.2(Li_2Zn_2O_3), \tag{5.1}$$

where *x* is the parameter of varying Li and Zn composition and also serves as a parameter for electron hole doping. $x = 0$ represents full unpaired electron occupancy per Mo_3O_{13} cluster, while $x = 1$ represents totally empty occupancy. The Li and Zn occupancy of the actual reacted products did not correlate with *x* in a way that was originally intended. This will be shown in the following results.

The starting ingredients for Type A recipe are Mo, MoO_2, MoO_3, Li_2MoO_4, and ZnO. The principle for using also MoO_3 as a starting ingredient lies in the fact that Zn_3Mo3O_8 can be synthesized using MoO_3 as one of the ingredients [22]. As $LiZn_2Mo_3O_8$ and Zn_3Mo3O_8 have the same space group and a similar atomic structure it was thought that $Li_{1-1}Zn_{2+x}Mo_3O_8$ is a hybrid of the two compounds and could be synthesized combining MoO_3 along with MoO_2. There is no proof to support this principle of mixing the recipes of two similar compounds. This was also tested by combining recipes of $Zn_2Mo_3O_8$ and $LiZn_2Mo_3O_8$, but that turned out to be unsuccessful.

The solid-state reaction of Type A recipe was done as explained previously, but a final reaction temperature of 1050 °C was used (except that for $x = 0.4$ sample it was 1000 °C). The first attempt with Type A was $x = 0.5$ followed by $x = 0.4$ and $x = 0.6$. Later, a remake of the $x = 0.5$ sample was done to see if it and the corresponding experimental data were reproducible or not. This sample will be referred to as $x = 0.5$ remake.

5.3 Type B $LiZn_2Mo_3O_8$ recipe

Behind the Type B $LiZn_2Mo_3O_8$ recipe there was an idea that lithium could be substituted by zinc so that Li + Zn = 3. In the Type A recipe, lithium tended to be more prone

to react into the final product than zinc. Because the Type A recipe has a target formula with a component of excess 0.2($Li_2Zn_2O_3$), there is always plenty of lithium available. Consequently, the desired imperfect occupation of Li and Zn could not be achieved in Type A samples. To solve this, in the Type B recipe the excess component holds only a little amount of lithium resulting in a target formula of

$$Li_{1-x}Zn_{2+x}Mo_3O_8 + 0.025(Li_2O) + 0.375(Zn_2O_2). \quad (5.2)$$

Starting ingredients are ZnO, Li_2MoO_4, Mo, and MoO_2. The final temperature in the reaction sequence was 1050 °C. Two samples of Type B recipe were done, with x = 0.25 and x = 0.5, respectively.

5.4 $Zn_2Mo_3O_8$ non-magnetic reference sample

It was found in Type A and Type B samples that they contained a second phase of $Zn_2Mo_3O_8$. Therefore, a reference sample of this non-magnetic compound was decided to be synthesized with a six-gram sample size. The preparation method was exactly the same as for $LiZn_2Mo_3O_8$ but with a final temperature of 1050 °C and with three percent excess ZnO according to Ref. [8]. The initial XRD of the product showed impurity peaks. After the HCl wash and 50 micron meshing, several but not all of the peaks disappeared from the XRD data. In Figure 21 a Rietveld fit of the HCL washed and meshed $Zn_2Mo_3O_8$ XRD is shown.

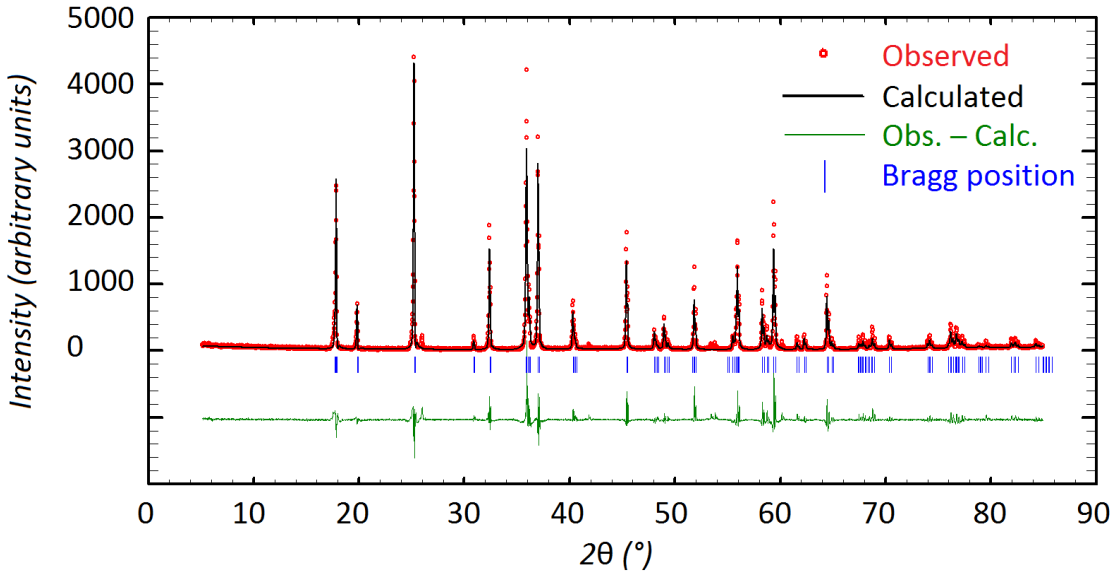

Figure 21. *Rietveld fit of the non-magnetic reference sample Zn2Mo3O8.*

The fit is not satisfactory with R-factors = 18.0 and 23.6, and χ^2 = 5.33. A few impurity peaks are still visible after the HCl wash. The MPMS measurement yielded one or two order of magnitude smaller susceptibility than in the $LiZn_2Mo_3O_8$ samples, in which case the effect of the background could not be ruled out. Therefore, the $Zn_2Mo_3O_8$ sample could be safely considered as non-magnetic.

5.5 Dependence on the Li/Zn hole doping

The Li/Zn hole doping study by altered $LiZn_2Mo_3O_8$ solid state reaction recipes had two purposes: to find a recipe for a stoichiometric lithium and zinc occupation and to see the effects on lattice constants and on the magnetic behavior. In the scope of this thesis work a total of seven successful samples of $LiZn_2Mo_3O_8$ were made. They are summarized in Table 2. The first is the reference $LiZn_2Mo_3O_8$, followed by four Type A and two Type B samples.

Table 2. *Summary of samples made for the Li/Zn ratio.*

Sample $LiZn_2Mo_3O_8$	**Li**	**Zn**	**a (Å)**	**c (Å)**	**2. phase (%)**	***C_1***
Reference	1.46(3)	1.58(1)	5.78551(9)	31.0620(6)		0.1379(6)
A, x = 0.4	0.9(4)	1.89(2)	5.80136(5)	31.1105(4)	2.4(1)	0.304(5)
A, x = 0.5	1.0(2)	2.12(2)	5.80381(5)	31.1109(4)	6.4(4)	0.378(10)
A, x = 0.6	1.3(2)	2.006(13)	5.80681(5)	31.1128(5)	13.3(3)	0.364(8)
A, x = 0.5 remake	1.0(3)	1.946(14)	5.80449(5)	31.1115(4)	10.3(3)	0.327(7)
B, x = 0.25	1.5(9)	1.81(2)	5.80030(5)	31.1105(5)	34.3(4)	0.226(3)
B, x = 0.5	1.8(4)	2.06(3)	5.80988(7)	31.1208(6)	44.3(5)	0.235(4)

In Table 2 starting from left to right, the first column is the name of the powder sample or what recipe it was made with. The second and third columns are the Li and Zn occupation summed up from 4–5 lattice sites. The lithium occupancy could not be reliably determined with XRD only, which is why they have a large margin of error and are marked as red. Then the table shows the lattice constants a and c. Most samples had a second phase of non-magnetic $Zn_2Mo_3O_8$. Therefore, the Rietveld analysis was performed with two sets of Bragg positions. Based on the intensity of the main and secondary phase it was possible to estimate the amount of the secondary phase. This is shown as a percentage in the table. All these crystallographic values and their margins of error where obtained from Fullprof [25] for most of the samples and from GSAS [28] for the reference $LiZn_2Mo_3O_8$ sample. The final column in the table is the Curie constant C_1 from the 200–300 K temperature range which is obtained by the inverse susceptibility from the MPMS experiments. The margin of error comes from the least square method of the fit.

The desired zinc occupancy (Zn = 2 + x) does not seem to be achieved by the Type A and B recipes when the zinc occupancies are more or less close to two. Therefore, the doping dependence analysis has to be done with a narrower range of zinc occupancy that originally intended. For the best stoichiometric compound almost all Type A and B compounds are good candidates. However, the Type A recipe is clearly superior to the Type B recipe in terms the secondary phase. The amount of secondary phase seems to increase as x gets larger in both Type A and B. When comparing the Type A samples

with x = 0.5 and x = 0.5 remake it seems that Type A samples are reproducible with some deviations.

The lattice constants a, b and c offer a way to evaluate or confirm the lithium and zinc composition with Vegard's law. The lattice constants are measured quite accurately by the XRD, but the method based on Vegard's law is only an estimation. In Figure 22 lattice constants from Table 2 and Table 1 are plotted as a function of the zinc occupancy to see if some kind of Vegard's law trend or other useful information could be observed. Corresponding plots for lithium dependency have not been made because of the lack of NPD data for most samples.

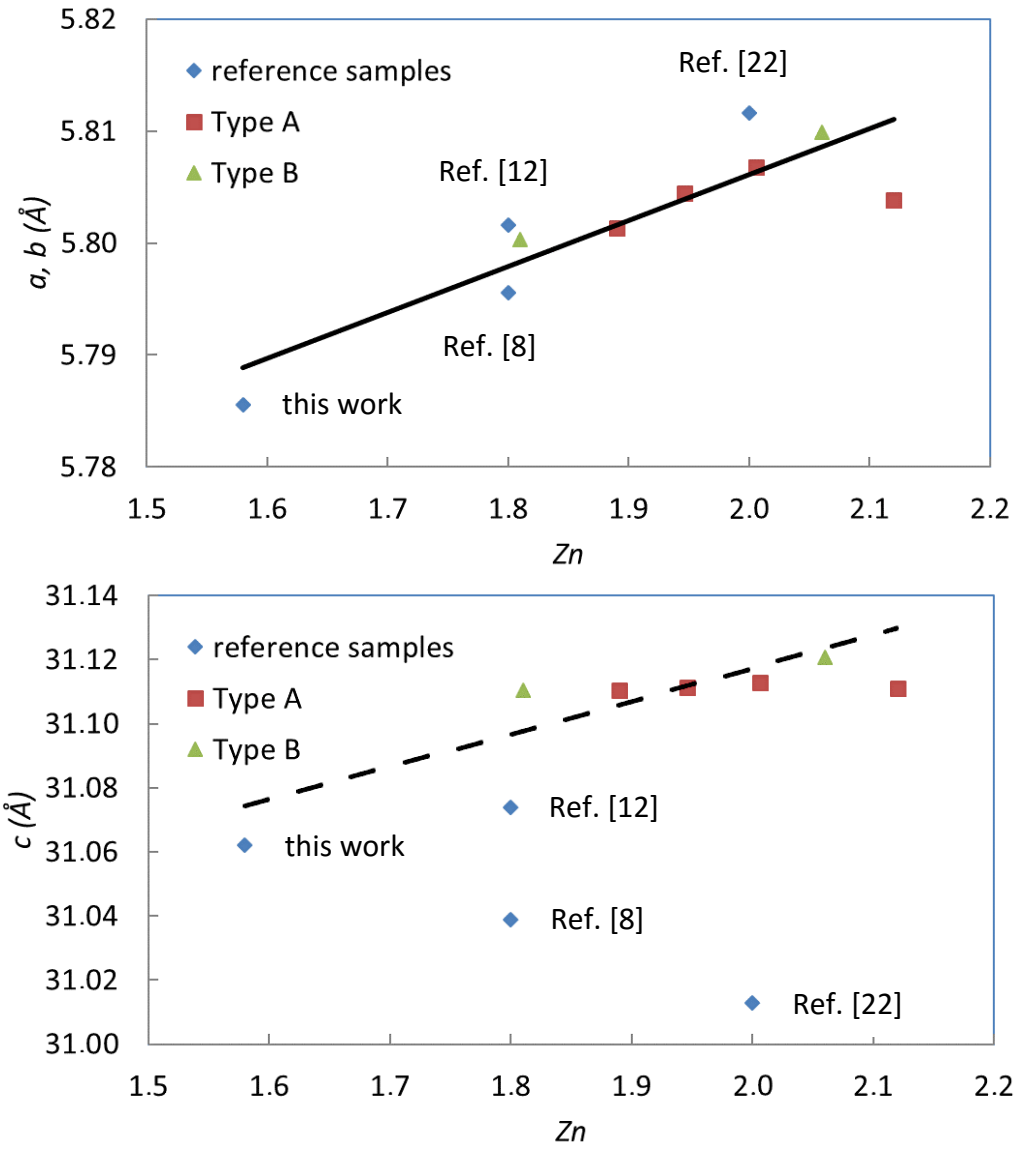

Figure 22. *Lattice constant dependency on the zinc concentration in $LiZn_2Mo_3O_8$ samples. Upper panel: Constants a and b. Lower panel: Constant c.*

The blue marks show the results for the literature samples and the reference $LiZn_2Mo_3O_8$ sample from this work. Each reference data point is individually marked

besides the corresponding blue mark. Type A samples are marked as red while type B with green. The upper panel shows the zinc occupancy dependency on the lattice constant *a* and *b*, while the lower panel shows the zinc dependency on the constant *c*. The zinc concentration dependence on *a* and *b* lattice constants seems to follow Vegard's law for experimental and literature data, which is seen as a linear fit in the upper panel of Figure 22. This seems to be true also for the lattice constant *c*, expect for that the literature values do not seem to follow the same relation as for the Type A and B samples. Therefore, the literature values are omitted from the lower panel fit (dashed line) in Figure 22. The linear fit results are

$$a = [5.72(2) + \mathrm{Zn} * 0.041(9)]\ \text{Å}, \tag{5.3}$$

$$c = [30.93(5) + \mathrm{Zn} * 0.09(3)]\ \text{Å}, \tag{5.4}$$

for lattice constants *a* and *c*, respectively. Here Zn is the zinc occupancy which determines the values of the lattice constants. Thus, the ideal lattice constants with Zn = 2 are *a* = 5.81(4) and *c* = 31.11(10). The error bars are rather large when compared for example to the accuracy of powder XRD. The future NPD + XRD Rietveld results will hopefully improve these results as the information of lithium occupancies becomes available. The slope/lattice constant relation is more than two times larger for lattice constant *a* than for *c*. This is counterintuitive with the idea that the Mo_3O_8 planes would make the lattice rigid in directions of *a* and *b*, while not restraining the direction of lattice constant *c*. This seems not to be the case.

The Curie constant C_1 is used to estimate the occupation of the spin magnetic moment per Mo_3 cluster. A Curie constant of 0.375 is required for a full occupancy. This offers another way to estimate the Li and Zn occupation, as lithium and zinc donate the unpaired spin magnetic moment to Mo_3O_{13} clusters. The Curie constants are not compensated for the non-magnetic second phase, so the values for the main phase would be larger in most of these samples. In Figure 23 the zinc dependence of Curie constant C_1 is presented.

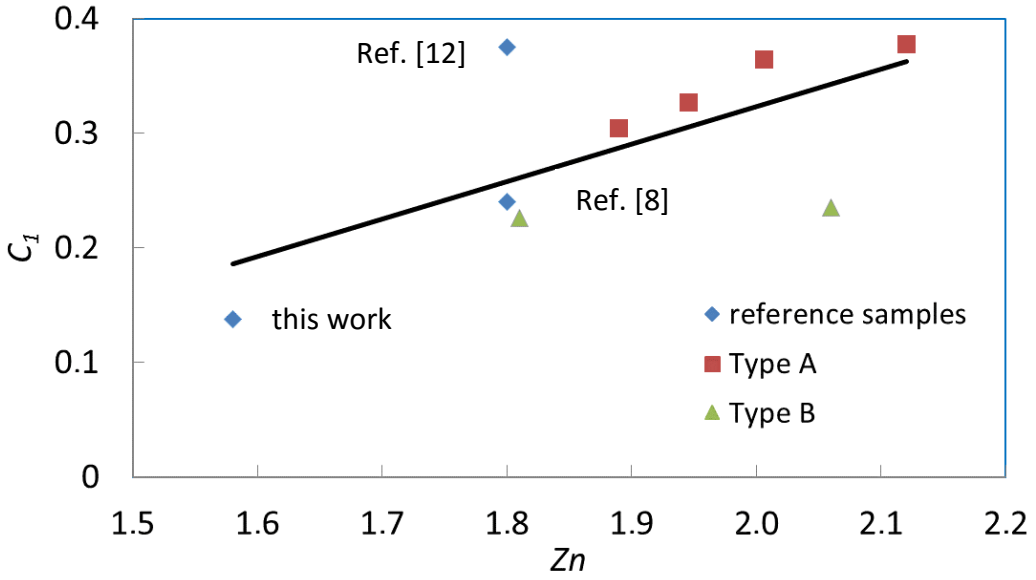

Figure 23. *Curie constant C_1 dependency on the zinc concentration. Blue marks are reference samples from the literature and this work. Red and green marks are from Type A and B samples.*

There seems to be a trend in the Curie constant C_1. However, it is difficult to compare the literature data because different kinds of methods were used to estimate the diamagnetic contributions χ_0. All the Curie constants and temperatures obtained from the inverse susceptibly curves are presented in Table 3 to serve as a reference for future studies.

Table 3. *Summary of Curie values for the LiZn2Mo3O8 reference and Type A and Type B samples.*

Sample $LiZn_2Mo_3O_8$	***C_1***	***T_{C1}* (K)**	***C_2***	***T_{C2}* (K)**
Reference	0.1379(6)	-121(1)	0.0703(4)	-11.8(2)
A, x = 0.4	0.304(5)	-501(9)	0.0442(4)	-10.0(4)
A, x = 0.5	0.378(10)	-652(18)	0.0400(4)	-8.5(4)
A, x = 0.6	0.364(8)	-739(17)	0.0339(4)	-7.4(4)
A, x = 0.5 remake	0.327(7)	-648(15)	0.0355(4)	-8.0(4)
B, x = 0.25	0.226(3)	-402(6)	0.0426(4)	-9.5(4)
B, x = 0.5	0.235(4)	-520(8)	0.0333(3)	-6.6(4)

All the Curie temperatures are negative which is a sign of an antiferromagnet. Curie temperatures are useful when determining the frustration parameter [18]. The three samples with the largest Curie constants C_1 also show anomalous kinks in the magnetic susceptibility. These are shown in Appendix A: magnetic susceptibilities of Type A $LiZn_2Mo_3O_8$ samples. This kind of an anomaly has previously not been reported for $LiZn_2Mo_3O_8$. An explanation for the kink could be that the antiferromagnetic coupling

of the unpaired spins temporarily slightly reduces the magnetization when lowering the temperature from the paramagnetic phase to the antiferromagnetic phase.

5.6 Single-crystal growth

A total of five single-crystal growth attempts were made, of which the final attempt was successful. They were all done with the solid-state reaction method. All the attempts are described in detail below in order to serve as a guideline for future studies.

The first and the second attempt were two samples of three grams with stoichiometric starting ingredient ratio for $LiZn_2Mo_3O_8$. For these samples the same kind of preparation as for the powder sample were used. Also the reaction sequence was the same, except that the final temperature was for the first sample 1150 °C for 5 days and for the second sample 1100 °C for 10 days. Both samples had a water quench performed as usually, and both sample vessels broke in the quench process. The tubes were probably weakened during the heating due to crystallization of the glass. As much as possible of the two samples were tried to be saved. After these samples it was decided that for a single-crystal growth there is no need for a water quench. Therefore, a five-hour slow cooling was done instead of a water quench for the following crystal growth attempts. The first sample was examined by a microscope. Figure 24 shows a single-crystal with dimensions of 500x300 microns.

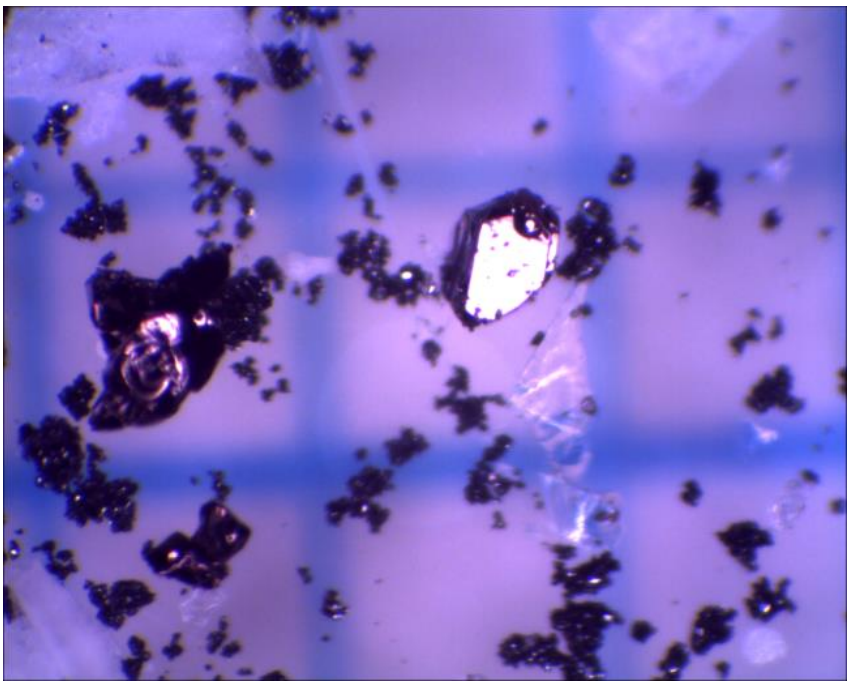

Figure 24. *Microscope picture of a single-crystal. The distances between the blue lines are one millimeter.*

A few crystals were picked up and a series of 4-axis X-ray measurements were performed for three crystals. The (0 0 6) reflection could not be found, but peaks with slightly larger 2θ were observed. They could be $Zn_2Mo_3O_8$ (0 0 2) reflections.

MPMS of one of the crystals with a mass of about 0.1–0.2 mg was measured. There was a problem to find the sample position at first. However, using temperature of 2 K and magnetic field of five Tesla the sample centering could be done and the measurement started. The maximum magnetization was about five times too small compared to the powder sample (considering the sample size). Also negative magnetization after 10 Kelvin was observed.

These experiments indicated no evidence of $LiZn_2Mo_3O_8$. Therefore, a third attempt of making a single-crystal was started by using the single-crystal recipe of how the $LiZn_2Mo_3O_8$ compound was initially found [22]. In this recipe, Li_2MoO_4, ZnO, and MoO_2 have a ratio of 1:2:5, which will make a shortage of zinc and a multiphase product is expected. The reaction sequence was in 1100 °C for five days and the amount was four grams. After the reaction, the quartz tube had shattered and the silica wool powderized. In this reaction, preservation in 600 °C for 24 hours was not done. That could have resulted in too quick vaporization of lithium. It would have then reacted with silica leading to breaking.

The fourth $LiZn_2Mo_3O_8$ single-crystal attempt was started with the same recipe as the third sample. The 600 °C lithium relaxation phase was once again included, and a peak temperature of 1050 °C for five days was selected. After the reaction, the silica tube had exploded, but the crucible was unharmed. The sample did not come out without breaking the crucible. A part of the sample was used for powder XRD to verify if $LiZn_2Mo_3O_8$ exists or not in the sample. A quick comparison to previous powder pattern data did not yield any matching peaks.

Success

The decomposition temperature of MoO_2 in 1100 °C could be responsible for building up vapor pressure, especially when there was a large amount of MoO_2 in the starting composition. A sealed molybdenum tube as described in Ref. [22] would deal with the pressure issue and it was used for the fifth sample.

Four grams of the sample, as in the two previous samples, was prepared. The molybdenum crucible was sealed inside a vacuum by using an arc furnace. The crucible was then sealed in a silica glass tube and put into the furnace. A final temperature of 1100 °C for two days without the 600 °C relaxation was used. After the reaction the molybdenum crucible was opened using a lathe. The pellet came out as one piece, and it weighed 3.71 grams. The crystals were also gathered from the sides of the crucible and several single-crystals were picked up for later experiments.

In order to verify that one of the picked crystals was of the desired compound $LiZn_2Mo_3O_8$, 4-axis XRD was performed. A final power of 1800 W for the X-ray source was used. A course φ–χ scan shown in Figure 25 reveals a large peak and three smaller peaks in the (0 0 6) range.

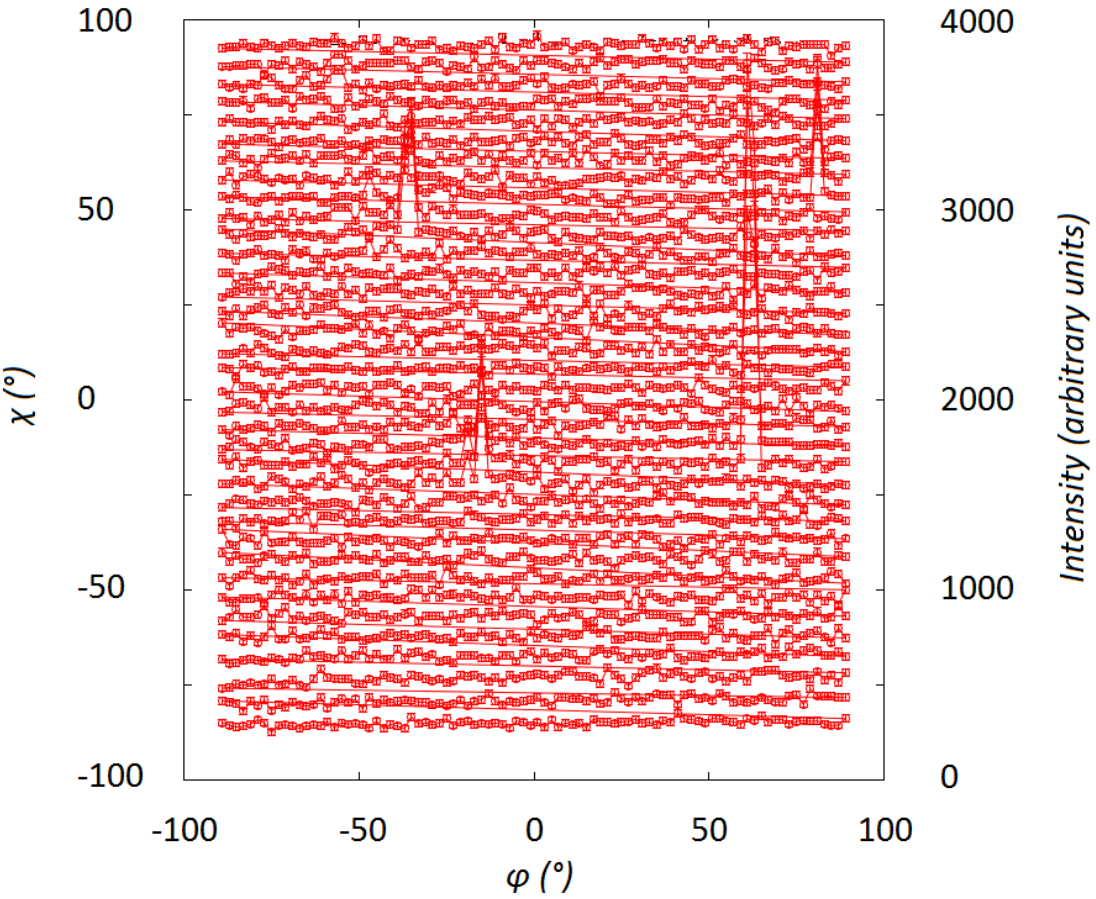

Figure 25. *φ–χ -scan in the 2θ range of (0 0 6) for a single-crystal of the fifth $LiZn_2Mo_3O_8$ preparation attempt.*

In Figure 25 the x-axis is φ with data ranging from -90° to 90°, while the y-axis is χ with data ranging from -85° to 90°. The y-axis displays also the intensity. When doing refining scans of the peak positions, 2θ of the large peak was 7.9195, while for the three smaller peaks it was 8.4444, 8.4435, and 8.4084, respectively. The large peak corresponds to (0 0 6), while the small peaks correspond to (0 1 2) reflection of $LiZn_2Mo_3O_8$. The multiplicity of the latter reflection is two, while for the former it is six. This is in agreement with the number of peaks found. The extinction rule was measured, in other words a 2θ-ω scan along (0 0 6) and the largest intensity (0 1 2) direction. (0 0 18) and (0 3 6) peaks were used to refine the χ and φ coordinates of these directions. The scans are presented in Figure 26 for (0 0 6) and in Figure 27 for (0 1 2).

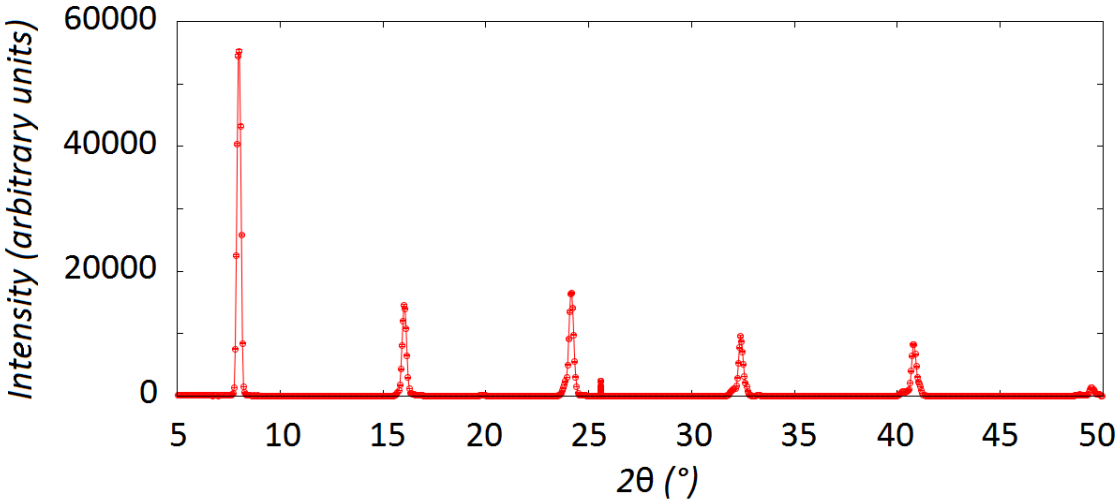

Figure 26. *2θ-ω scan along (0 0 6) for the largest peak of Figure 25.*

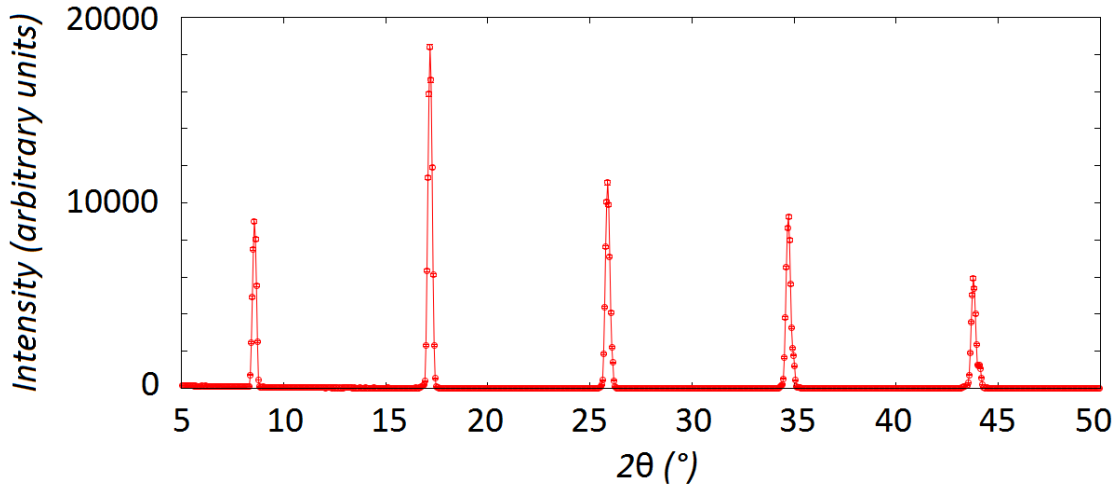

Figure 27. *2θ-ω scan along (0 1 2) for one of the three smaller peaks with the largest intensity of Figure 25.*

Both Figure 26 and Figure 27 are intensity plots as a function of 2θ. Using Bragg's law the data in Figure 26 yields c = 30.52(3) for the lattice constant. Based on the trigonometry of the (0 1 2) direction the lattice constant a is obtained from

$$a = \frac{1}{2}\frac{dc}{\sqrt{\frac{1}{4}c^2 - d^2}}\cos^{-1}\frac{\pi}{6}, \tag{5.5}$$

where d is the distance between the (0 1 2) planes obtained from the data in Figure 27 using Bragg's law. The cosine term is a correction factor for the hexagonal lattice. This yields a = 5.778(8). The existence of a single-crystal of $LiZn_2Mo_3O_8$ is not supported by the too small value of lattice constant c, in contrast with being plausible in terms of lattice constant a. This result could be due to an incorrect determination of peak positions. The angles χ and φ were only refined with the third order peaks (0 0 18) and (0 3 6), while this could have been done in the sixth and fifth order to improve accuracy.

MPMS measurement was done for the largest single-crystal found from the fifth sample. Its dimensions were roughly 900x500x100 microns and it was weighed to be 0.32(2) mg. In Figure 28 the inverse susceptibility of this crystal of is shown.

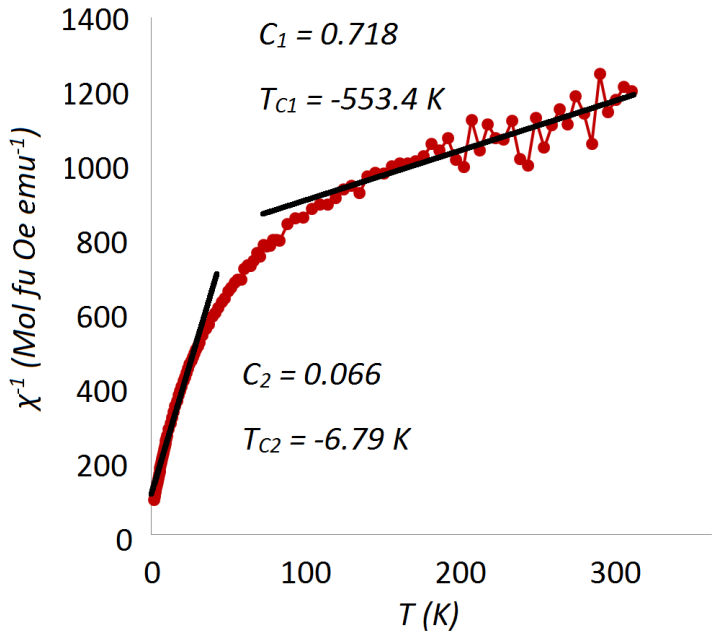

Figure 28. *Sinle-crystal magnetic susceptibility from the fifth single-crystal attempt in a magnetic field of one Tesla.*

The Curie constant C_1 was found to be 0.718, which is twice the value of fully occupied spin 1/2 magnetic moments. The diamagnetic contributions were not subtracted. However, doing this would only increase the Curie constant values. It has to be considered that a crystal of this size has other sources of significant errors which should be taken into account. As a meaningful result, the single-crystal has a clear magnetic signal, which gives support that it is *not* the non-magnetic $Zn_2Mo_3O_8$.

6. CONCLUSIONS

The compound $LiZn_2Mo_3O_8$ is a resonating valence bond (RVB) state candidate. The goal for studying this compound is to verify the existence of such a quantum mechanical state for the first time. In order to prepare good $LiZn_2Mo_3O_8$ samples for this purpose, the scope of this thesis work has been to reproduce and improve the previous literature results of powder-sample synthesis and single-crystal growth.

The initial attempts to reproduce the reference $LiZn_2Mo_3O_8$ powder sample were partly successful. The right compound could be synthesized, but the same experimental results from magnetic measurements as in Ref. [8] could not be obtained. However, the reference sample in this thesis work and in the literature reference samples are not perfect when it comes to the stoichiometric occupation of lithium and zinc atoms. From temperature NPD experiments done on the reference sample it is suggested that no structural phase transition occurs between 3–300 Kelvin, which is in agreement with previous experimental work. Small movement of lithium lattice positions were observed, but it is difficult to conclude if they had considerable significance in this study.

Two modifications of $LiZn_2Mo_3O_8$ powder sample recipes were made in order to find a stoichiometric sample and to study the dependence of Li and Zn hole doping, known as Type A and Type B recipes. Neither of them yielded the desired occupancies of zinc. However, this turned out not to be a problem. Type A recipe seems to be plausible for making stoichiometric $LiZn_2Mo_30_8$, while also providing some variation in the zinc occupation. Type B recipe seems also good for this purpose, but it contains too much secondary phase compared to Type A. However, lithium occupations have to be measured in order to clarify of the usefulness of Type A and B recipes.

Compared to the reference sample, the Type A and B samples had Curie constants closer to the ideal 0.375 value of fully occupied spin magnetic moments. This is another indication that Type A and B recipes can yield more perfect lithium and zinc occupations in $LiZn_2Mo_30_8$ samples. An anomalous magnetic susceptibility behavior in the 100–200 K region was observed for the Type A $x = 0.5$, $x = 0.5$ remake, and $x = 0.6$ samples. These samples are exposed to antiferromagnetic coupling of the unpaired spins that temporarily slightly reduces the magnetization when lowering the temperature from the paramagnetic phase. This magnetic behavior has not been previously reported for $LiZn_2Mo_30_8$.

The single-crystal attempts finally yielded a successful growth of $LiZn_2Mo_30_8$ single-crystals, although this is yet to be verified. The 4-axis X-ray diffraction experiment was

incomplete, and its results do not suggest the correct lattice constant *c* value for the $LiZn_2Mo_3O_8$ compound. However, the susceptibly of a 0.32 mg large single-crystal from the same sample clearly indicates magnetic behavior.

In future research there are two focus points. The first is to verify and find the maximally perfect stoichiometric powder sample of $LiZn_2Mo_30_8$. This will be done with the help of neutron powder diffraction. Then it will be possible to perform various experiments on this sample, for example high magnetic field measurements and inelastic neutron scattering to find information about the possible frustrated state. The second point is to find and refine a method for growing a large single-crystal. Even with small single-crystals some experiments will be possible. Powder crystal and single-crystal experiments will support each other. However, the ultimate goal is to obtain a large, let us say in the range of one-gram single-crystal for inelastic neutron scattering to obtain the best possible experimental evidence for the RVB state.

REFERENCES

[1] L. Balents, Spin liquids in frustrated magnets, Nature, Volume 464, March 2010, p. 199–208.

[2] G. H. Wannier, Antiferromagnetism. The Triangular Ising Net, Physical Review, Volume 79, Number 2, July 1950, p. 357–364.

[3] P.W. Anderson, Resonating valence bonds: A new kind of insulator? Material Research Bulletin, Volume 8, February 1973, p. 153–160.

[4] S. Nakatsuji, Y. Nambu, H. Tonomura, O. Sakai, S. Jonas, C. Broholm, H. Tsunetsugu, Y. Qiu, Y. Maeno, Spin disorder on a triangular lattice, Science, Volume 309, September 2005, p. 1697–1700.

[5] J. S. Helton, K. Matan, M. P. Shores, E. A. Nytko, B. M. Bartlett, Y. Yoshida, Y. Takano, A. Suslov, Y. Qiu, J.-H. Chung, D. G. Nocera, Y. S. Lee, Spin dynamics of the spin-1/2 Kagome lattice antiferromagnet ZnCu3(OH)6Cl2, Physical Review Letters, Volume 98, Article 107204, March 2007.

[6] K. Matan, T. Ono, Y. Fukumoto, T. J. Sato, J. Yamaura, M. Yano, K. Morita, H. Tanaka, Pinwheel valence-bond solid and triplet excitations in the two-dimensional deformed kagome lattice, Nature Physics, Volume 6, November 2010, p. 865–869.

[7] J. N. Reimers, A. J. Berlinsky, A.-C. Shi, Mean-field approach to magnetic ordering in highly frustrated pyrochlores, Physical Review B, Volume 43, Number 1, January 1991, p. 865–878.

[8] J. P. Sheckelton, J. R. Neilson, D. G. Soltan, T. M. McQueen, Possible valence-bond condensation in the frustrated cluster magnet LiZn2Mo3O8, Nature Materials, Volume 11, Issue 6, June 2012, p. 493–496.

[9] R. Flint, P. A. Lee, Emergent Honeycomb Lattice in LiZn2Mo3O8, Physical Review Letters, Volume 111, November 2013, Article 217201.

[10] M. Mourigal, W. T. Fuhrman, J. P. Sheckelton, A. Wartelle, J. A. Rodriguez-Rivera, D. L. Abernathy, T. M. McQueen, C. L. Broholm, Molecular Quantum Magnetism in LiZn2Mo3O8, Physical Review Letters, Volume 112, Issue 2, Article 027202, January 2014.

[11] J. P. Sheckelton, F. R. Foronda, L. D. Pan, C. Moir, R. D. McDonald, T. Lancaster, P. J. Baker, N. P. Armitage, T. Imai, S. J. Blundell, T. M. McQueen, Local magnetism and spin correlations in the geometrically frustrated cluster magnet LiZn2Mo3O8, Physical Review B, Volume 89, Article 064407, February 2014.

[12] J. P. Sheckelton, J. R. Neilson, T. M. McQueen, Electronic tunability of the frustrated triangular-lattice cluster magnet LiZn2-xMo3O8, Materials Horizons, Volume 2, Issue 1, January 2015, p. 76–80.

[13] Y. Haraguchi, C. Michioka, M. Imai, H. Ueda, K. Yoshimura, Spin-liquid behavior in the spin-frustrated Mo3 cluster magnet Li2ScMo3O8 in contrast to magnetic ordering in isomorphic Li2InMo3O8, Physical Review B, Volume 92, Article 014409, July 2015.

[14] G. Chen, H.-Y. Kee, Y. B. Kim, Cluster Mott insulators and two Curie-Weiss regimes on an anisotropic kagome lattice, Physical Review B, Volume 93, Article 245134, June 2016.

[15] K. Sandvik, D. Okuyama, M. Avdeev, T. J. Sato, Unpublished manuscript.

[16] G. N. Lewis, The atom and the molecule, Journal of the American Chemical Society, Volume 38, Number 4, April 1916, p. 762–785.

[17] W. Heitler, F. London, Wechselwirkung neutraler Atome und homöopolare Bindung nach der Quantenmechanik, Volume 44, Issue 6, 1927, p. 455–472.

[18] A. P. Ramirez, Strongly geometrically frustrated magnets, Annual Review of Materials Science, August 1994, Volume 24, p. 453–480.

[19] MATLAB Release 2015b - academic use, The MathWorks, Inc., Natick, Massachusetts, United States.

[20] P.W. Anderson, The resonating valence bond state in La2CuO4 and superconductivity, Science, Volume 235, March 1987, p. 1196–1198.

[21] B. Lake, D. A. Tennant, C. D. Frost, S. E. Nagler, Quantum criticality and universal scaling of a quantum antiferromagnet, Nature Materials, Volume 4, April 2005, p. 329–334.

[22] C. C. Torardi, R. E. Mccarley, Synthesis, crystal-structures, and properties of LiZn2Mo3O8, Zn3Mo3O8, and ScZnMo3o8, reduced derivatives containing the Mo3O13 cluster unit, Inorganic Chemistry, Volume 24, Issue 4, 1985, p. 476–481.

[23] M. M. Abd-Elmeguid, B. Ni, D. I. Khomskii, R. Pocha, D. Johrendt, X. Wang, K. Syassen, Transition from Mott Insulator to Superconductor in GaNb4Se8 and GaTa4Se8 under High Pressure, Physical Review Letters, Volume 93, Number 12, Article 126403, September 2014.

[24] K. Momma, F. Izumi, VESTA 3 for three-dimensional visualization of crystal, volumetric and morphology data, Journal of Applied Crystallography, Volume 44, December 2011, p. 1272–1276.

[25] J. Rodríguez-Carvajal, Recent developments of the program FULLPROF, Commission on powder diffraction (IUCr). Newsletter, Volume 26, December 2001, p. 12–19.

[26] R. C. Jaklevic, J. Lambe, A. H. Silver, J. E. Mercereau, Quantum Interference Effects in Josephson Tunneling, Physical Review Letters, Volume 12, Number 7, February 1964, p. 159–160.

[27] G. Shirane, S. M. Shapiro, J. M. Tranquada, Neutron Scattering with a Triple-Axis Spectrometer, Cambridge university press, Published 2002, Printed 2006

[28] A.C. Larson, R.B. Von Dreele, General Structure Analysis System (GSAS), Los Alamos National Laboratory Report LAUR 86–748, 2004.

[29] B. H. Toby, EXPGUI, a graphical user interface for GSAS, Journal of Applied Crystallography, Volume 34, April 2001, p. 210–213.

APPENDIX A: MAGNETIC SUSCEPTIBILITIES OF TYPE A $LIZN_2MO_3O_8$ SAMPLES

The magnetic susceptibilities of the Type A samples (see Sec. 5.5) are shown in Figures 29–31. In the range of 100–200 K there are small anomalous kinks shown in the zoomed insets of each figure.

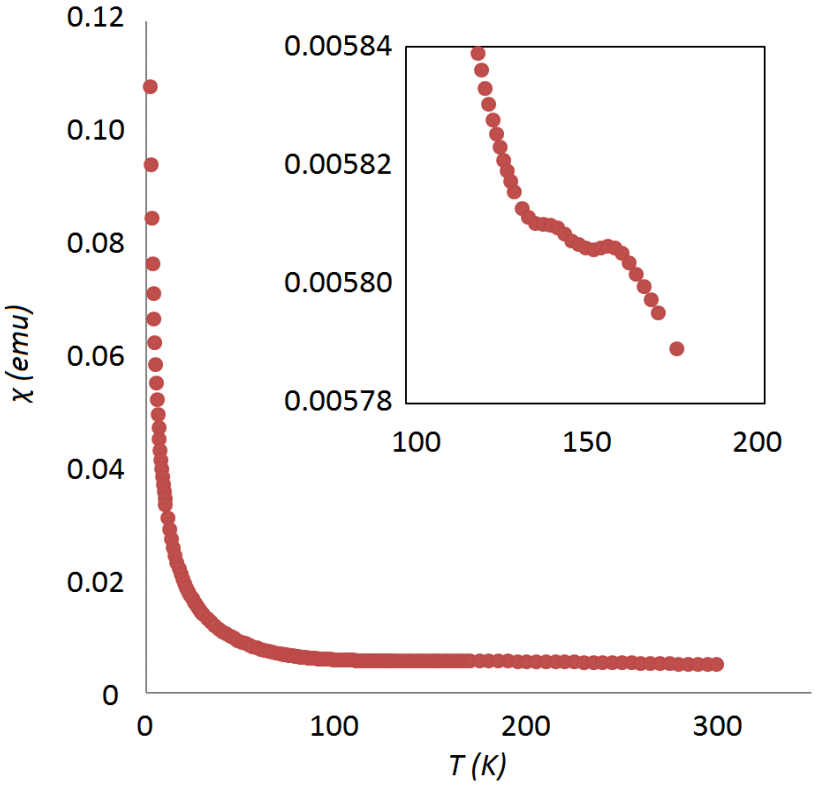

Figure 29. *Susceptibility of type A, x = 0.5 remake sample.*

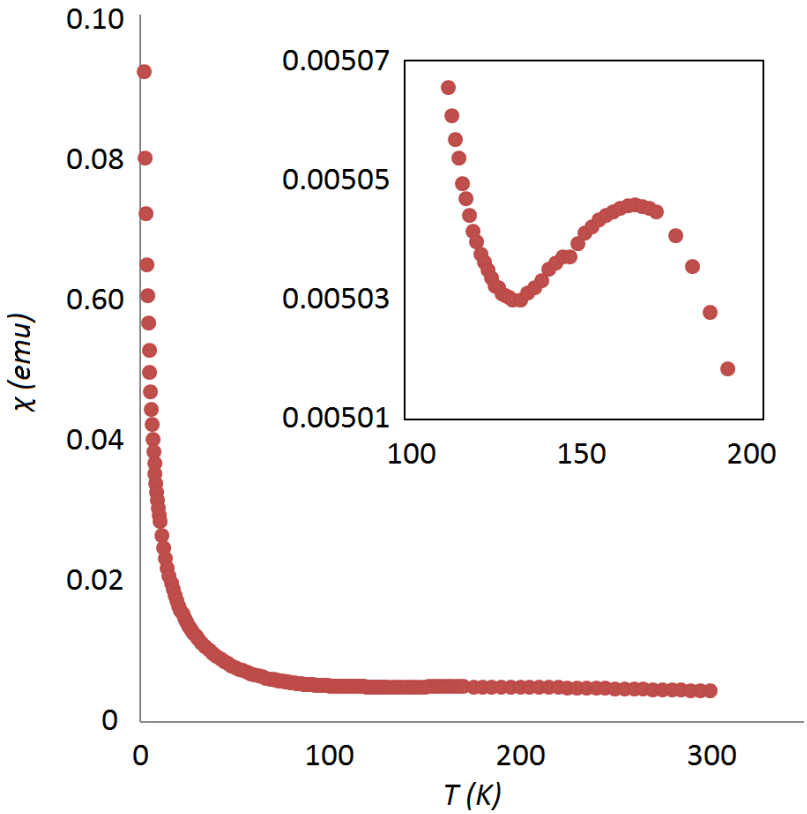

Figure 30. *Susceptibility of type A, x = 0.5 sample.*

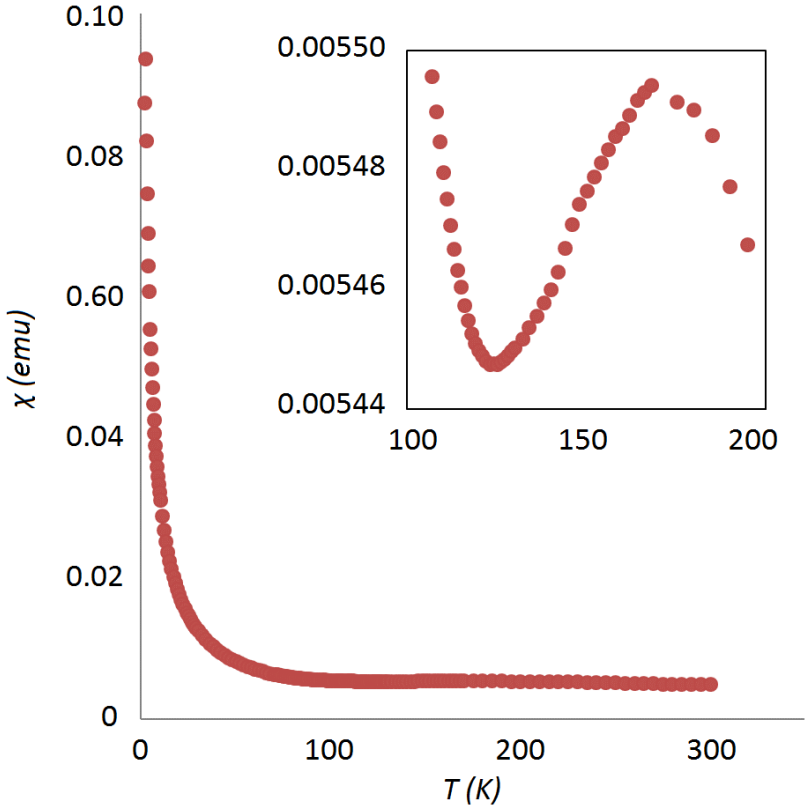

Figure 31. *Susceptibility of type A, x = 0.6 sample.*